Journal of Asian Earth Sciences 236 (2022) 105319

Contents lists available at ScienceDirect

Journal of Asian Earth Sciences

journal homepage: www.elsevier.com/locate/jseaes

Controls of the paleoenvironment on differential organic matter enrichment of lacustrine fine-grained rocks: A case study of the Jurassic Da'anzhai Member, central Sichuan Basin, SW China

Ziyi Liu [a,b], Dongxia Chen [a,b,*], Wenzhi Lei [a,b], Yang Liu [c,*], Guangjie Xie [b], Wei Dang [d], Xiuxiang Lv [a,b], Sha Li [a,b], Siyu Yuan [e]

[a] *State Key Laboratory of Petroleum Resources and Prospecting, China University of Petroleum, Beijing 102200, China*
[b] *College of Geosciences, China University of Petroleum, Beijing 102200, China*
[c] *School of Energy Resource, China University of Geosciences (Beijing), Beijing 100083, China*
[d] *School of Earth Sciences and Engineering, Xi'an Shiyou University, Xi'an 710065, China*
[e] *Hubei Institute of Geosciences, Wuhan 430034, China*

ARTICLE INFO

Keywords:
Organic matter accumulation
Clastic input
Sedimentation rate
Clastic dilution
Organic matter oxidation

ABSTRACT

Organic matter (OM) is not only a source of oil and gas but also the dominant host for hydrocarbon storage in unconventional reservoirs; thus, understanding the controls on OM accumulation are of great significance for unconventional hydrocarbon exploration. Lacustrine fine-grained rocks of the Jurassic Da'anzhai Member have variable total organic carbon (TOC) contents ranging from 0.11 to 3.11 wt%. However, it is still debatable regarding mechanisms responsible for such variable enrichment. Here, we present petrological, organic, and elemental geochemical data of three wells in the Jurassic Da'anzhai Member in the central Sichuan Basin, South China. The low enrichment of redox-sensitive trace elements (Mo_{EF}, U_{EF}, and V_{EF}) in lacustrine fine-grained rocks indicates oxic to suboxic conditions during deposition of the Da'anzhai Member, which are not conducive to OM preservation. The chemical index of alteration (CIA) values vary between 75 and 100, suggesting a warm/hot and humid paleoclimate. Relatively high productivity coincides with high CIA, suggesting that weathering fluxes may have played important role in the regulating primary productivity. Furthermore, the relationship between TOC and $(La/Yb)_N$ implies the influence of specific sedimentation rates on OM enrichment. Our results suggest that the OM accumulation in the Jurassic Da'anzhai Member is mainly controlled by clastic input and sedimentation rate. We propose that under conditions of variable clastic input, the appropriate sedimentation rate may have played a key role in the accumulation of OM. Finally, our study suggests that the siliceous shale may be a potential lithology for unconventional hydrocarbon production in the Jurassic Da'anzhai Member.

1. Introduction

Fine-grained rocks, including mudstone, shale, oil shale, clay rock, marl, siltstone, argillaceous siltstone, and other rock types, can be divided into various types according to grain size and sedimentary structure (Krumbein, 1932; Speight, 2013; Yuan et al., 2015). The total organic carbon (TOC) content of fine-grained rocks usually varies significantly in unconventional reservoirs. For example, as an important target stratum for shale oil production in the United States, the Bakken shale in the Williston Basin is characterized by a sandwich-like sedimentary structure (Sonnenberg and Pramudito, 2009; Peischl et al., 2016). Siliceous shales were mainly deposited in the upper and lower parts of the Bakken Member, with average TOC values ranging from 2.0 wt% to 12.0 wt% (Sonnenberg and Pramudito, 2009). The Ordovician Wufeng and Silurian Longmaxi Formations are the main source rocks of marine shale gas in Sichuan Basin, China (Chen et al., 2011; Guo, 2014; Dai et al., 2014; Hu et al., 2017; Yang et al., 2017b). The fine-grained rocks of the Wufeng-Longmaxi Formation consist of shale as well as a set of fine clastic rocks such as siltstone (Liang et al., 2012; Guo et al., 2017). Among them, the Lower Member 1 of the Longmaxi shale (1.0 wt% ≤ TOC ≤ 6.0 wt%) has been considered as the main production horizon of shale gas (Hu et al., 2017; Guo et al., 2017; He et al., 2018; Sun

---

* Corresponding authors at: State Key Laboratory of Petroleum Resources and Prospecting, China University of Petroleum, Beijing 102200, China (D. Chen). School of Energy Resource, China University of Geosciences (Beijing), Beijing 100083, China (Y. Liu).

E-mail addresses: lindachen@cup.edu.cn (D. Chen), yangliu@cugb.edu.cn (Y. Liu).

https://doi.org/10.1016/j.jseaes.2022.105319
Received 18 November 2021; Received in revised form 10 June 2022; Accepted 22 June 2022

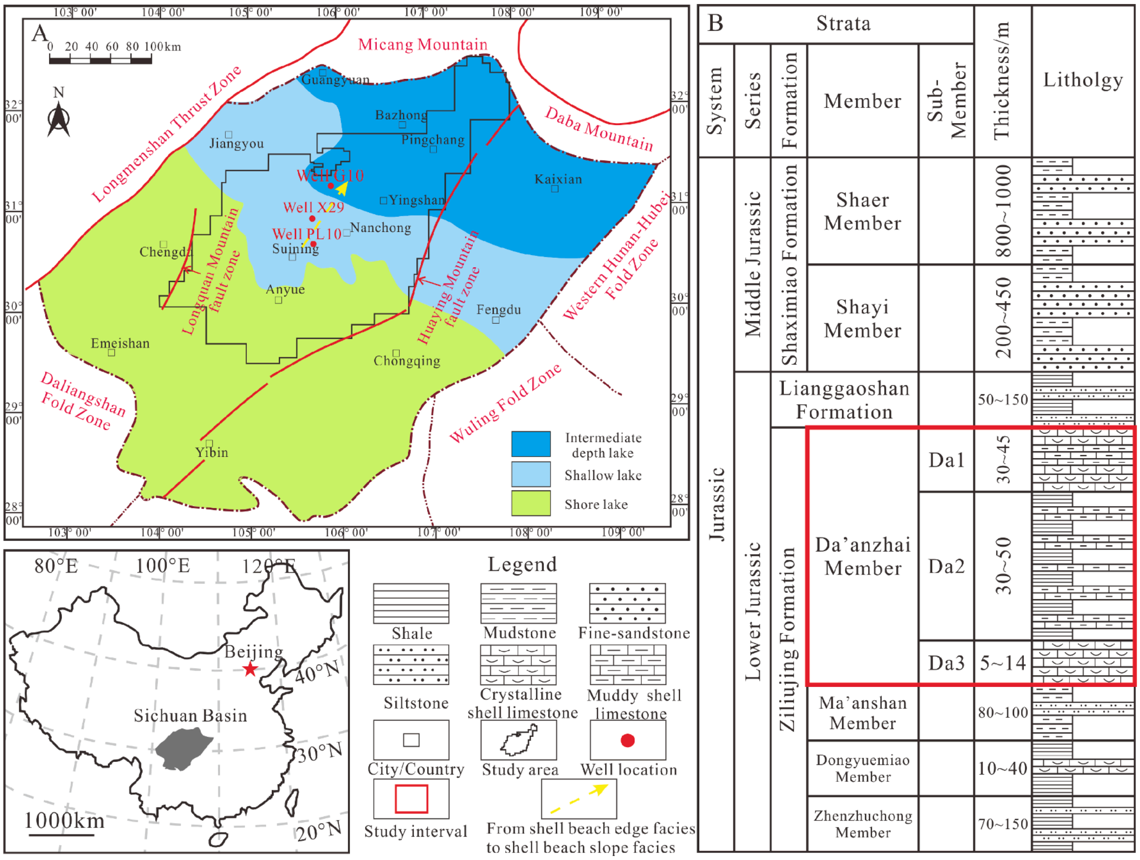

Fig. 1. (A) Location of the study area in the Sichuan Basin, China; (B) simplified stratigraphic units of the Jurassic system in the central Sichuan Basin.

et al., 2021).

Given that organic matter (OM) typically provides hydrocarbon storage, and organic-rich fine-grained rocks contain a considerable proportion of natural gas and oil (Raiswell et al., 1988; Jones and Manning, 1994; Hu et al., 2017; Guo et al., 2017; Blood et al., 2019), a clear understanding of OM enrichment is therefore important. Generally, the accumulation of OM is controlled by various sedimentary paleoenvironmental factors, including paleoredox conditions, paleoproductivity, clastic input and sedimentation rate (Ibach, 1982; Collins et al., 1995; Rimmer et al., 2004; Ding et al., 2015; Jin et al., 2020; Song et al., 2021). The lithological assemblage, sedimentary structures, biomarkers, isotopic compositions, and chemical elements in fine-grained rocks can provide valuable information on the sedimentary paleoenvironment (Macquaker and Adams, 2003; Jarvie et al., 2007; Nelson, 2009; Chermak and Schreiber, 2014; Schieber, 2016; Yang et al., 2019). For example, special minerals (e.g., syngenetic pyrites) in sediments can reveal the paleoredox conditions (Wilkin et al., 1996; Blood et al., 2019; Liu et al., 2019). Iron speciation, stable isotopes (e.g., S and C) and redox-sensitive trace elements (e.g., Mo, U, and V) have also been widely used to reconstruct the water column redox conditions (Elderfield and Greaves, 1982; Johannesson et al., 1994; Tribovillard et al., 2006; Goldberg et al., 2007; Scott et al., 2008; Pi et al., 2013; Jin et al., 2016; Liu et al., 2020). Elements such as P, Cu, Ni, and Zn are widely used as proxies for paleoproductivity (Tribovillard et al., 2006; Scott et al., 2017; Zhang et al., 2019; Yu et al., 2021). Additionally, Al is considered the principal conservative proxy for clay mineral flux in fine-grained clastic deposits (Blood et al., 2019), and its concentration can be used to reflect clastic input (Ross and Bustin, 2009; Jin et al., 2020). The $(La/Yb)_N$ ratio could act as a proxy for the sedimentation rate (Elderfield and Greaves, 1982; Johannesson et al., 1994). OM enrichment in different sedimentary basins may be controlled by one or several factors. For example, previous studies have proposed a relationship between the TOC content and sedimentation rate under stable clastic input conditions, which revealed that TOC tends to increase and then decrease as the sedimentation rate increases (Ibach, 1982; Collins et al., 1995; Tyson, 2001; Ding et al., 2015). This phenomenon is controlled by clastic dilution and OM oxidation. However, the influence of changes in the clastic input during the sedimentary process should also be considered. When the clastic input content varies, the sedimentation rate responds accordingly and may become appropriate for OM enrichment.

In ancient lakes, OM accumulation depends on production, preservation, and clastic dilution, where production is associated with productivity, and preservation is controlled by water chemistry, and/or sedimentation rate. In the study area, OM is generally accumulates in fine-grained rocks with TOC values higher than 1.0 wt%. Previous studies have proposed that OM accumulation in the Jurassic Da'anzhai Member was controlled by redox conditions (Xu et al., 2017a; Qiu and He, 2021; Lei et al., 2021). Xu et al. (2017a) suggested that conditions were oxic–suboxic during the Da'anzhai Member deposition. Conversely, the V/(V + Ni) ratios suggest that they were deposited under anoxic bottom water conditions (Qiu and He, 2021; Lei et al., 2021).

In this study, sedimentary paleoenvironmental parameters are discussed to reveal the mechanism of differential OM enrichment. Among them, unstable clastic inputs are considered in the relationship between the TOC content and sedimentation rate. First, the provenance of the main mineral matrix in fine-grained rocks was determined through major and trace elements and fine-grained rock characteristics. Second, the sedimentary paleoenvironment of fine-grained rocks was revealed through the characteristics of shells, paleoredox conditions, paleoproductivity, clastic input, and sedimentation rate. Finally, by combining the provenance of the main mineral matrix in fine-grained rocks with the factors affecting OM enrichment, the OM enrichment conditions in different lithologies and sedimentary facies were determined.

2. Geological setting

The Sichuan Basin is among the most significant oil- and gas-producing regions in China. The study area is bounded by the Huaying Mountain to the east and Longquan Mountain to the west. The northern part extends to the front of Micang and Daba Mountains (Fig. 1A). The Da'anzhai Member of the study area is the most important oil and gas production layer in the Jurassic strata of the Sichuan Basin (Fig. 1B, Yang et al., 2017a; Xu et al., 2020). The Da'anzhai Member is a set of lacustrine deposits, which is divided into the Da1 (30–45 m), Da2 (30–50 m), and Da3 (about 5–14 m) submembers from top to bottom (Fig. 1B, Xu et al., 2017b; Zou et al., 2019). The fine-grained rocks consist of crystalline shell limestones (coquina), muddy shell limestones, and shales (Fig. 1B). Crystalline shell limestones are mainly found in the Da1 and Da3 submembers, and the muddy shell limestones and shales were mainly deposited in the Da2 submember. Biological shells can be found in shale as well as in limestone and are commonly found in shell beach core facies. Affected by lake waves and storm waves, the shells are distributed from the shell beach core facies to the shell beach slope facies in different shapes (Feng et al., 2015; Fick et al., 2018).

In addition to the tight oil found in typical lacustrine tight limestone (Tian et al., 2017; Xu et al., 2020), shales in the Jurassic Da'anzhai Member can act as unconventional reservoirs of shale gas and oil (Xu et al., 2017b; Zou et al., 2019). The TOC content in the shales ranges from 0.5 wt% to 4.3 wt% and the thermal maturity (R_o) varies from 0.75% to 1.57%, with that of the main body exceeding 1.0% (Yang et al., 2017a; Zou et al., 2019). Additionally, the OM in the Da'anzhai Member is classified as Type II (Xu et al., 2017b; Zou et al., 2019). To understand the differential OM enrichment mechanism of fine-grained rocks in the Da'anzhai Member, three wells (PL10, well X29, and well G10) were selected from the shell beach edge facies to the shell beach slope facies (Fig. 1A).

3. Samples and methods

To reveal the characteristics of fine-grained rocks from the Da'anzhai Member in the central Sichuan Basin, 68 core samples were collected from wells PL10, X29, and G10. The core samples in each well were mainly from Da2 submember. All samples were selected for X-ray diffraction (XRD) analysis, which is sufficient to present the mineral characteristics of different lithologies in the study area; samples of different lithologies were observed under a transmitted light microscope. In addition to the samples from well X29, those analyzed using a carbon analyzer were also subjected to rock pyrolysis experiments. The T_{max} values were obtained for wells PL10 and G10. Finally, 48 core samples (including different lithologies from each well) were analyzed for major, trace, and rare earth elements.

3.1. XRD

Mineral content was determined using a Bruker D8 Discover X-ray diffractometer (Chalmers and Bustin, 2008). Initially, the core samples were crushed and centrifugally separated to a particle size smaller than 10 μm. Subsequently, a bulk composition of the powdered samples was analyzed to determine the total clay content. Finally, a finer sample fraction was analyzed to determine the individual mineral content (Liu et al., 2018; Liu et al., 2021). The analytical uncertainty was typically less than 5%.

3.2. TOC and T_{max}

The TOC values of the core samples were determined using a LECO CS-230 carbon analyzer at the China University of Petroleum (Beijing, China). To remove inorganic carbon, the core samples were crushed and sieved through an 80-mesh sieve and reacted with 10 vol% HCl for 1 h. The measurement precision was estimated as 0.45% of the measured TOC value. Rock pyrolysis was performed using a Rock-Eval 6 pyrolysis apparatus at the Experimental Research Center of the Wuxi Institute of Petroleum Geology, China. During the experiment, 60 mg of pulverized samples was heated at a constant rate (25 °C/min) until the temperature reached 650 °C (Carvajal-Ortiz and Gentzis, 2015). OM gradually releases hydrocarbons in different heating processes. The peak temperature (T_{max}) of the pyrolytic hydrocarbon S_2 was obtained.

3.3. Microscopic analyses

The characteristics of fine-grained rocks, including shape and distributions of shells or carbonate, were observed on polished samples using a Leica 4500P microscope and transmitted light at the China University of Petroleum (Beijing, China).

3.4. Major, trace, and rare earth elements

The major oxides and trace and rare earth elements of the selected samples were analyzed at the National Institute of Natural Hazards, China. For major element analyses, the selected samples were ground into 200-mesh pieces and melted into glass frits. An Axios AX X-ray fluorescence (XRF) spectrometer was used to measure the major element oxides in the glass frit. The test temperature was 23 °C, and the process followed the national standard "GB/T 14506.28–2010." The analytical precision of XRF spectrometry was better than 5%. For trace and rare earth element analyses, the samples were dissolved in HF (30%) and HNO_3 (68%) at 190 °C for 24 h. After evaporating the excess solvent at 130 °C for 3 h, the samples were redissolved in 2 mL of 6 mol/L HNO_3 in capped Teflon bombs at 150 °C for 48 h (Chen et al., 2020). Then, trace element analysis was carried out using an Element XR inductively coupled plasma mass spectrometer (ICP-MS) based on the Chinese National Standard GB/T 14506.30–2010. The accuracy of this analysis was better than ±5% for most elements.

The chemical index of alteration (CIA) has been widely used to reflect the chemical weathering of source areas and climatic changes (Nesbitt and Young, 1982; Chen et al., 2019). The CIA can be calculated as follows: $CIA = \text{molar } [(Al_2O_3)/(Al_2O_3 + CaO^* + Na_2O + K_2O)] \times 100$, where CaO^* represents CaO in silicate minerals only (Nesbitt and Young, 1982, 1989). Here, CaO^* can be approximated using the following formula: $CaO^* = CaO - 10/3 \times P_2O_5$ (Mclennan, 1993). If the number of CaO^* moles is more than that of Na_2O, CaO^* is assumed to be equivalent to Na_2O (Mclennan, 1993; Chen et al., 2020). CIA values between 50 and 65 indicate weak chemical weathering in a cool-arid sedimentary climate. CIA values from 65 to 85 indicate medium chemical weathering in a warm-humid sedimentary climate, and values between 85 and 100 indicate intense chemical alteration in a hot and humid climate (Nesbitt and Young, 1982; Fedo et al., 1995; Xu et al., 2017a; Zhai et al., 2018; Yu et al., 2021). Additionally, the amount of diagenetic K_2O (K-metasomatism) was corrected using the Al_2O_3–(CaO^* + Na_2O)–K_2O (A–CN–K) ternary diagram (Fedo et al.,1995). This can also be calculated using the following formula: $K_2O\text{corr} = [m \times A + m \times (C^* + N)]/(1 - m)$, where $m = K/(A + C^* + N + K)$ for the protolith, and A, (C^* + N), and K represent the molar values of Al_2O_3, ($CaO^* + Na_2O$), and K_2O, respectively (Panahi et al., 2000; Rieuet al., 2007). The K- corrected CIA value is expressed as CIAcorr.

The element enrichment factors (Mo_{EF}, U_{EF}, V_{EF}, Cu_{EF}, Ni_{EF}, and Zn_{EF}) were calculated using the formula: $X_{EF} = (X/Al)_{sample}/(X/Al)_{AUCC}$, where X = Mo, U, V, Cu, Ni, or Zn; and AUCC refers to the composition of the average upper continental crust (McLennan, 2001). Additionally, the $(La/Yb)_N$ ratio can act as a proxy for the sedimentation rate. Here, N stands for North American Shale (NASC) standardization, and the NASC data are from Haskin et al. (1968). A $(La/Yb)_N$ ratio close to 1 corresponded to a high sedimentation rate. In contrast, the ratio indicates a low sedimentation rate (Zeng et al., 2015; Chen et al., 2019).

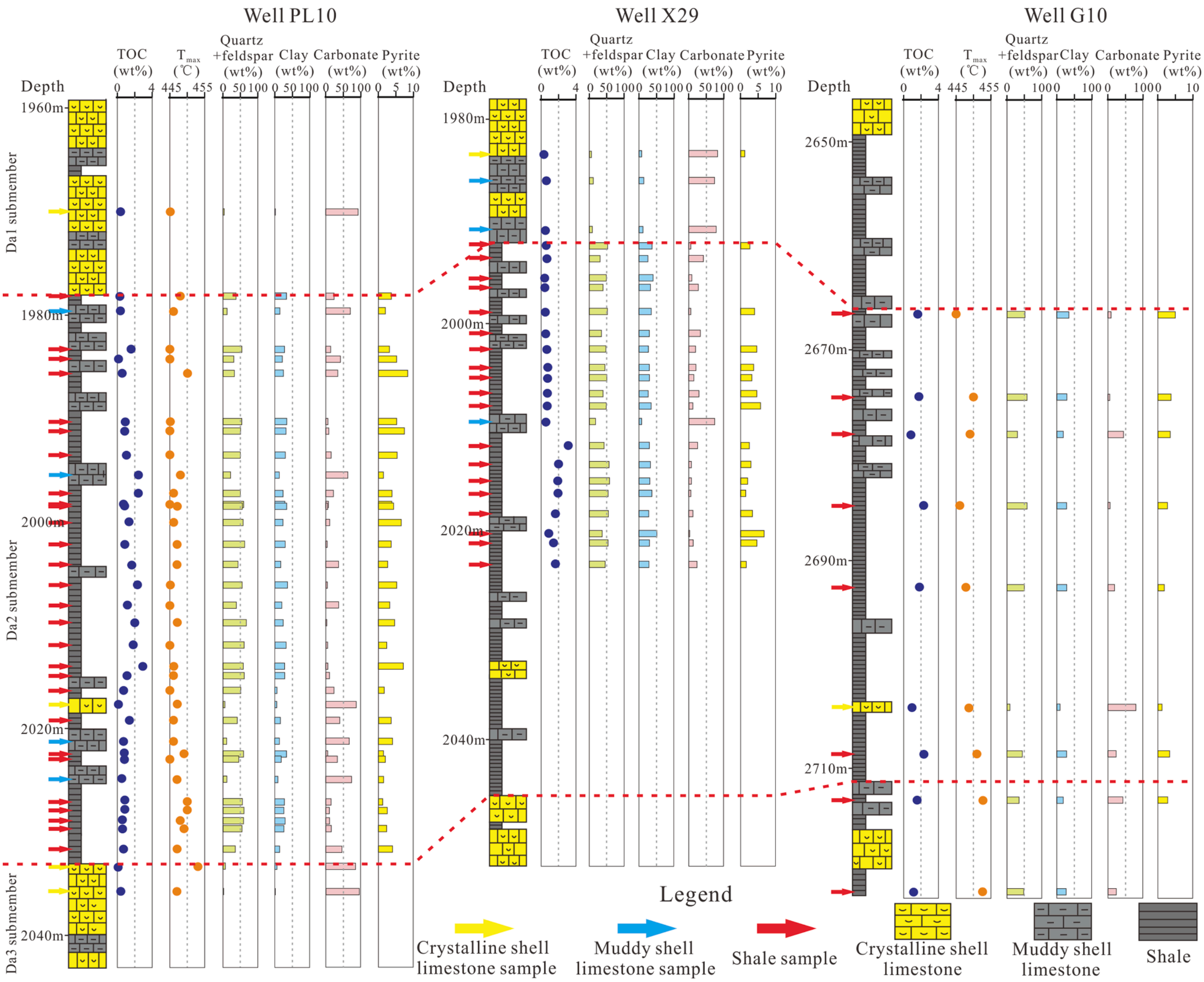

Fig. 2. Lithology and mineral constituents of wells PL10, X29, and G10.

4. Results

4.1. Petrology and mineralogy

The matrix in the fine-grained rocks is composed of siliceous, argillaceous, calcareous, and mixed minerals (Fig. 2). As shown in Fig. 3, siliceous and mixed shales were dominant. In the Da'anzhai Member, muddy shell limestones have carbonate contents ranging between 60 and 80 wt%, while those in the crystalline shell limestones are higher than 80 wt% (Fig. 2).

In crystalline shell limestone, the shells have a disorderly distribution in the sediments (Fig. 4A), and are filled with sparry calcite (Fig. 5A). Meanwhile, shells can appear in sediments as laminae (Fig. 4B, C, and 5B), and remobilization of both sediments and shells can be observed in muddy shell limestone (Fig. 4B and 5C). In addition to the shells, ostracods can also be found in mixed shales in a specific sedimentary environment (Fig. 4D and 5D). There are also some fine-grained rocks with few or no shells (Fig. 4E, F, and 5E). In fine-grained rocks, carbonate both as sparry calcite in the shells as well as recrystallized calcite laminae (Fig. 4C and 5F).

4.2. Bulk geochemistry

The TOC content of organic-rich shale is proposed to be higher than 1.0 wt% based on the evaluation of North American marine shale oil and gas "sweet spots." (Yang et al., 2015; Zou et al., 2019). In well PL10, the TOC content mainly ranges between 0.5 and 1.0 wt% in the Da2 submember and between 0.0 and 0.5 wt% in the Da1 and Da3 submembers (Fig. 6A). Similar distributions of TOC are also observed in well X29 (Fig. 6B). Compared to wells PL10 and X29, samples from well G10 have higher TOC values, with TOC contents of 1.0 to 2.0 wt% in the Da2 submember and 0.5 to 2.0 wt% in the Da1 and Da3 submembers (Fig. 6C). Generally, the TOC values of the Da2 submember are higher than those of the Da1 and Da3 submembers (Fig. 6A-C). As shown in Fig. 6D, 54% of the siliceous shale samples have TOC contents greater than 1.0 wt%, and more than 96% of samples have TOC contents higher than 0.5 wt%. TOC contents higher than 1.0 wt% are observed in 38% of the mixed shale samples, and 81% of the samples featured by TOC contents above 0.5 wt%. Compared to siliceous shales and mixed shales, limestones have low TOC contents, especially crystalline shell limestones, with 83% of the samples having TOC contents below 0.5 wt%. Additionally, there were a few samples of argillaceous shale, in which the corresponding TOC content was between 0.5 and 1.0 wt%. The siliceous and mixed shales have higher TOC contents than other fine-grained rocks in the study area (Figs. 2 and 6D). Most of the samples showed T_{max} values ranging from 445 to 450 ℃ (Fig. 2), which indicates a similar OM maturity in the samples.

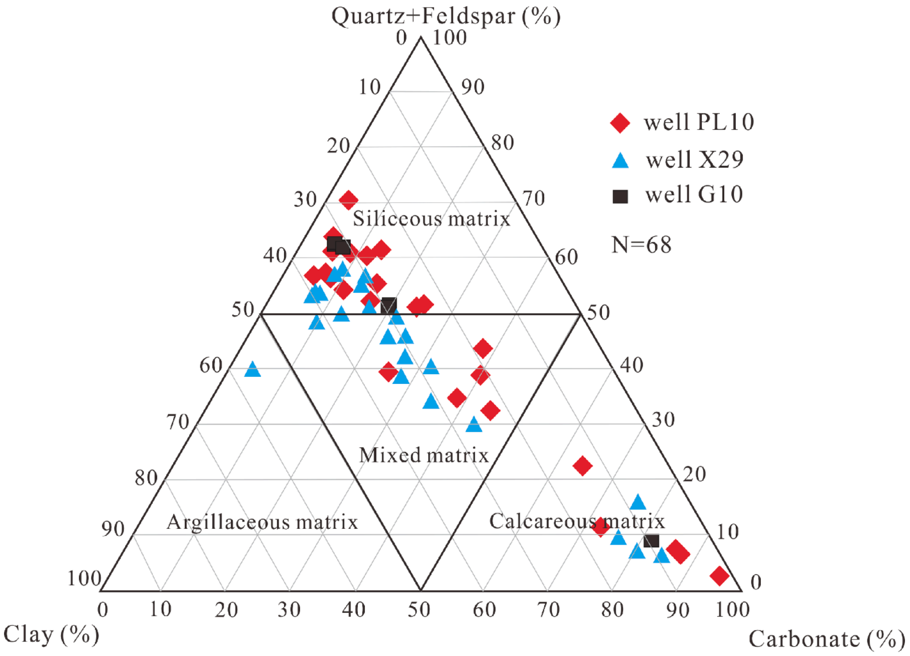

Fig. 3. Main mineral compositions and matrix types in fine-grained rocks.

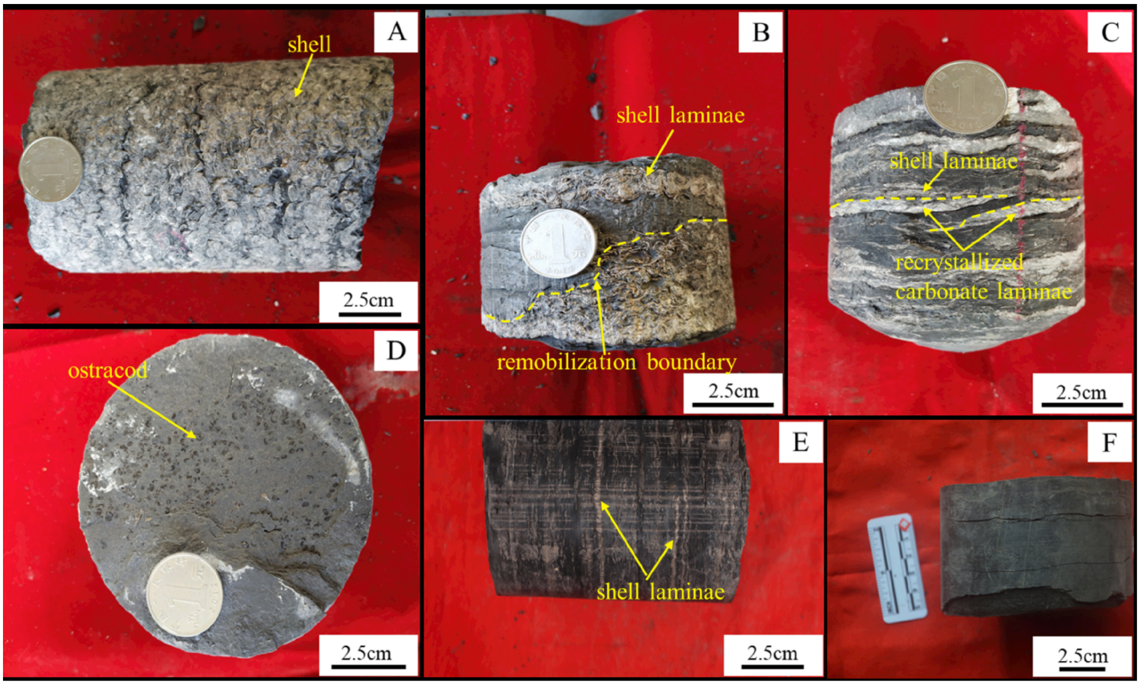

Fig. 4. Characteristics of core samples of fine-grained rocks from the Da'anzhai Member. (A) Crystalline shell limestone with many shells from well PL10, 1970.0 m; (B) remobilization of both sediments and shells in muddy shell limestone in well PL10, 1979.2 m; (C) shell laminae and recrystallized calcite laminae in muddy shell limestone in well PL10, 2021.1 m; (D) ostracods dispersed in mixed shale in well PL10, 2019.1 m; (E) shell laminae in mixed shale in well X29, 2023.1 m; (F) siliceous shale without shells in well G10, 2674.5 m.

4.3. Elemental geochemistry

The diagenetic K-metasomatism (conversion of kaolinite to illite) in fine-grained sediments may have affected the CIA values (Fedo et al., 2012). Theoretically, the weathering trend of the source rocks should be distributed along an ideal line parallel to the A–CN boundary, reflecting the concurrent losses in Na, Ca, and K. In the study area, samples exhibited a weathering trend deviating slightly from the ideal weathering line, indicating weak diagenetic K-metasomatism (Fig. A1). However, various studies have shown that the effect of K-metasomatism on first-order CIA value trends is insignificant even in ancient shale samples (Rieu et al., 2007; Zou et al., 2018; Zhai et al., 2018). Likewise, the CIAcorr values were similar to the CIA values in the study area (Fig. 7 and Table 1). Additionally, the lack of correlation between CIA values and provenance indicators (for example Al/Ti, Th/Sc, Fig. A2) suggests that CIA values can be robustly explained by changes in the intensity of chemical weathering (McLennan, 1993). To avoid variations in CIA caused by sorting during transport, only shales were used to evaluate

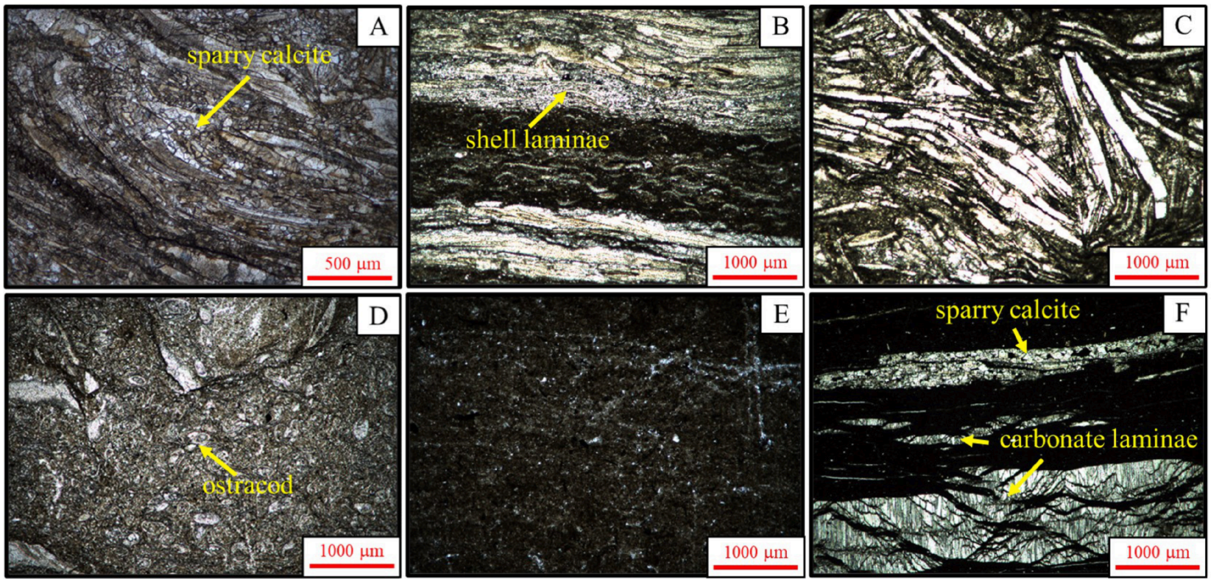

Fig. 5. Characteristics of fine-grained rocks under transmitted light (A–F) and SEM (G–I). (A) The shells in crystalline shell limestone are filled with sparry calcite in well PL10, 1970.0 m; (B) shell laminae in mixed shale with floating small shells between laminae in well X29, 2023.1 m; (C) remobilization of both sediments and shells in muddy shell limestone in well PL10, 1979.2 m; (D) ostracods dispersed in mixed shale in well PL10, 2019.1 m; (E) siliceous shale in well G10, 2674.5 m; (F) carbonate strips crystallize in muddy shell limestone, and sparry calcite fills in shells in well PL10, 2021.1 m.

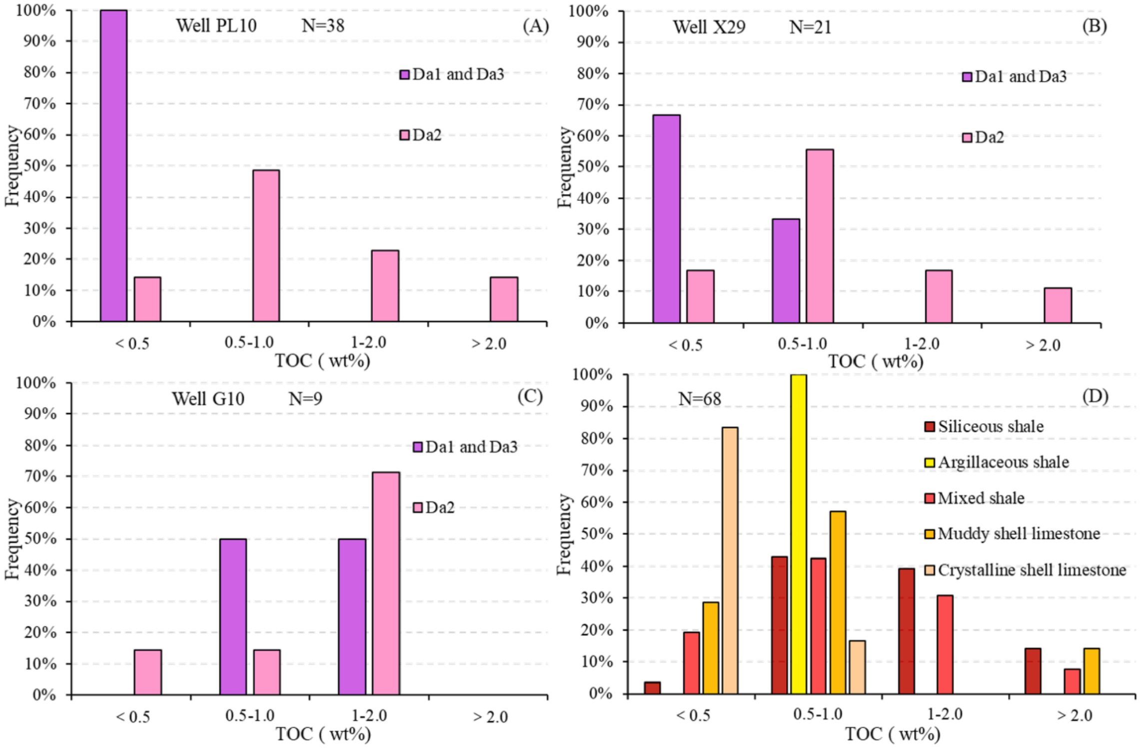

Fig. 6. TOC distribution in different submembers and lithologies. (A) TOC is mainly in the ranges of 0.5–1.0 wt% in the Da2 submember and the range of 0.0–0.5 wt % in the Da1 and Da3 submembers in well PL10; (B) TOC is mainly in the ranges of 0.5–1.0 wt% in the Da2 submember and 0.0–0.5 wt% in the Da1 and Da3 submembers in well X29; (C) TOC is mainly in the ranges of 1.0–2.0 wt% in the Da2 submember and 0.5–2.0 wt% in the Da1 and Da3 submembers in well G10; (D) TOC is mainly in the ranges of 0.5–1.0 wt% in shale and muddy shell limestone and 0.0–0.5 wt% in crystalline shell limestone.

climatic conditions. In the study area, shales were mainly deposited in Da2 submember. For well PL10, the CIA values range from 75.56 to 81.26 (mean = 78.87). Similar to well PL10, the CIA values range from 74.68 to 83.07 (mean = 79.25) in well X29 and from 76.20 to 81.29 (mean = 78.88) in well G10. Most CIA values were greater than 75 for the Da2 submember (Table 1 and Fig. 7).

To eliminate potential influences from changes in lithology or the detrital fraction, element enrichment factors were used for paleoredox (e.g., Mo_{EF}, U_{EF}, and V_{EF}) and paleoproductivity (e.g., Cu_{EF}, Ni_{EF}, and Zn_{EF}) interpretations, rather than the absolute concentrations of these elements. Redox-sensitive trace element (e.g., Mo, U, and V) and micronutrient (e.g., Cu, Ni, and Zn) concentrations in the Da'anzhai

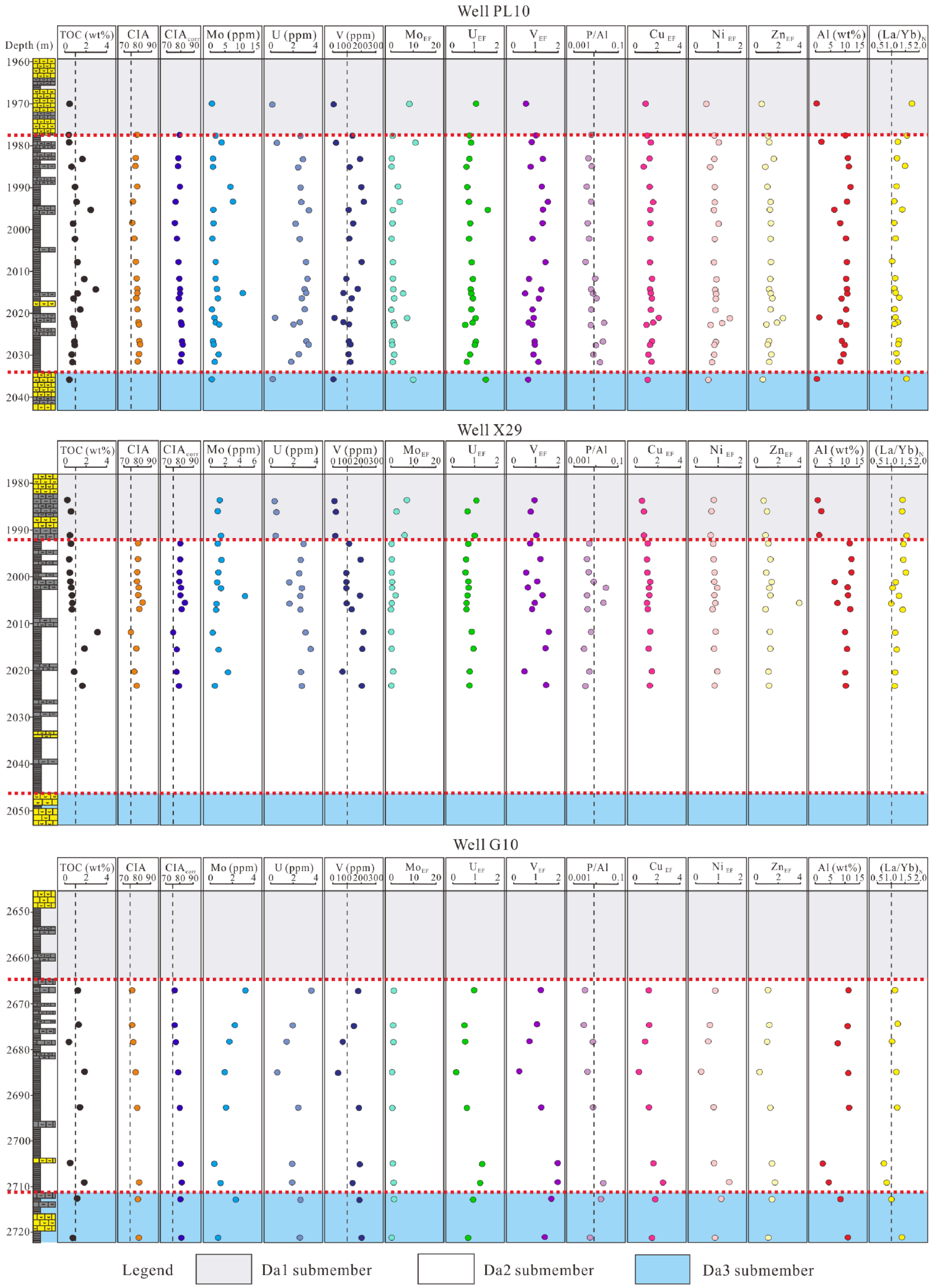

Fig. 7. Stratigraphic distributions of TOC, CIA, CIAcorr, paleoredox indicators (e.g., Mo_{EF}, U_{EF}, and V_{EF}), paleoproductivity indicators (e.g., P/Al, Cu_{EF}, Ni_{EF}, and Zn_{EF}), Al concentrations, and $(La/Yb)_N$ ratios in wells PL10, X29 and G10.

Member are presented in Table 2. Mo_{EF} varied from 0.18 to 10.71 (mean = 2.06), U_{EF} varied from 0.16 to 1.57 (mean = 0.82), and V_{EF} varied from 0.25 to 1.98 (mean = 1.04). In the Da'anzhai Member, there were relatively low Mo, U, and V concentrations with low element enrichment factors (Fig. 7). Additionally, Cu_{EF} varied from 0.19 to 1.46 (mean = 0.77), Cu_{EF} varied from 0.17 to 1.07 (mean = 0.61), and Zn_{EF} varied from 0.11 to 3.22 (mean = 1.01). Except for well G10, the micronutrient concentrations in Da1 and Da3 submembers are lower than those in Da2 submember (Fig. 7).

Strong discrepancies in the Al concentrations and $(La/Yb)_N$ ratios were also observed in the sediments. High Al concentrations may reflect an enhanced clastic input and/or reduced carbonate production. As shown in Tables 1 and 2, the Da1 and Da3 submembers in well PL10 showed Al concentrations varying from 0.34 to 0.38 wt% (mean = 0.36 wt%) and $(La/Yb)_N$ ratios with values of 1.53 to 1.57 (average of 1.55). Compared to well PL10, well X29 exhibited higher Al concentrations, with an average of 1.43 wt%, and lower $(La/Yb)_N$ ratios, with an average of 1.44. Among the Da1 and Da3 submembers of the selected wells, the

Table 1
TOC and major elements in the Da'anzhai Member.

Sub-Member	Samples	Depth	TOC (wt %)	Major elements													
				CaO (wt %)	P_2O_5 (wt %)	Al_2O_3 (wt %)	SiO_2 (wt %)	TiO_2 (wt %)	Na_2O (wt %)	K_2O (wt %)	Fe_2O_3 (wt %)	MnO (wt %)	Al (wt %)	Si/Si*	Al/Al*	CIA	CIAcorr
Da1	PL10-1	1970.0	0.38	70.93	0.12	0.72	1.98	0.08	0.10	0.08	2.08	0.16	0.38	0.02	0.19	n.d.	n.d.
Da2	PL10-2	1977.5	0.32	9.33	0.15	19.13	46.64	0.60	0.41	3.47	6.66	0.06	10.13	0.50	0.68	78.90	78.90
	PL10-3	1979.2	0.35	62.65	0.26	3.73	8.59	0.12	0.14	0.64	2.75	0.16	1.97	0.08	0.49	n.d.	n.d.
	PL10-4	1983.1	1.60	1.54	0.12	20.70	58.14	0.75	0.56	3.64	5.96	0.02	10.96	0.63	0.72	78.14	78.14
	PL10-6	1985.0	0.58	3.66	0.17	21.14	51.83	0.71	0.48	4.07	7.59	0.05	11.19	0.56	0.68	77.90	77.90
	PL10-7	1989.8	0.94	1.65	0.11	22.35	54.61	0.72	0.50	3.88	7.66	0.04	11.83	0.58	0.69	79.24	79.24
	PL10-9	1993.4	1.07	4.87	0.15	19.88	52.99	0.62	0.67	3.73	6.55	0.03	10.52	0.57	0.70	76.08	76.08
	PL10-10	1995.3	2.40	28.67	1.17	11.79	32.91	0.45	0.43	2.29	4.70	0.06	6.24	0.34	0.65	n.d.	n.d.
	PL10-12	1998.5	0.72	11.11	0.08	15.46	46.46	0.50	0.56	2.91	5.69	0.03	8.18	0.52	0.67	75.56	75.56
	PL10-15	2002.2	0.90	2.26	0.11	19.24	59.35	0.64	0.65	3.31	6.23	0.02	10.19	0.63	0.70	77.05	77.05
	PL10-18	2007.8	1.16	3.78	0.08	19.92	55.35	0.77	0.65	3.15	6.58	0.04	10.55	0.59	0.69	78.19	78.19
	PL10-20	2011.8	1.82	3.47	0.21	19.47	56.16	0.79	0.56	3.12	6.60	0.04	10.31	0.60	0.69	78.83	78.83
	PL10-21	2014.3	2.90	2.29	0.15	20.05	56.06	0.73	0.54	3.21	7.40	0.04	10.61	0.60	0.67	79.22	79.22
	PL10-22	2015.2	1.14	1.44	0.19	20.34	59.27	0.89	0.57	3.19	6.67	0.05	10.77	0.63	0.70	79.21	79.21
	PL10-23	2016.4	0.75	7.61	0.21	16.51	54.55	0.82	0.55	2.49	6.37	0.07	8.74	0.58	0.66	78.54	78.54
	PL10-25	2019.1	1.41	3.68	0.14	19.50	55.91	0.86	0.51	3.13	6.76	0.04	10.32	0.60	0.68	79.35	79.35
	PL10-26	2021.1	0.71	66.44	0.41	2.03	7.52	0.08	0.10	0.22	2.78	0.12	1.07	0.07	0.35	n.d.	n.d.
	PL10-27	2022.2	0.83	19.54	0.46	15.63	46.15	0.71	0.44	2.26	6.40	0.11	8.27	0.45	0.64	80.03	80.03
	PL10-28	2022.7	0.87	3.08	0.13	19.46	52.61	0.73	0.47	2.95	5.80	0.05	10.30	0.60	0.72	80.39	80.39
	PL10-30	2026.7	0.86	8.04	0.44	16.78	53.65	0.86	0.42	2.42	5.18	0.06	8.88	0.58	0.71	80.72	80.72
	PL10-31	2027.5	0.91	3.71	0.22	18.33	57.08	0.80	0.45	2.53	6.96	0.16	9.70	0.61	0.66	81.26	81.26
	PL10-33	2029.8	0.60	7.01	0.17	17.54	50.45	0.65	0.44	2.61	8.51	0.17	9.29	0.54	0.60	80.39	80.39
	PL10-34	2031.6	0.68	18.69	0.30	15.67	41.69	0.60	0.42	2.43	5.03	0.07	8.30	0.44	0.70	79.59	79.59
Da3	PL10-36	2035.8	0.40	74.22	0.15	0.64	1.72	0.03	0.09	0.08	1.95	0.11	0.34	0.01	0.19	n.d.	n.d.
Da2	G10-11	2667.0	1.25	2.25	0.08	20.93	54.18	0.73	0.71	3.87	7.30	0.09	11.08	0.59	0.68	76.20	76.20
	G10-12	2674.5	1.35	0.93	0.07	20.40	56.28	0.64	0.71	3.70	6.32	0.03	10.80	0.62	0.71	76.26	76.26
	G10-13	2678.3	0.46	18.58	0.12	14.09	38.67	0.43	0.47	2.42	4.25	0.03	7.46	0.43	0.71	77.15	77.15
	G10-15	2684.8	1.88	0.48	0.10	20.83	56.79	0.57	0.69	3.53	6.36	0.03	11.03	0.63	0.71	78.81	78.81
	G10-18	2692.6	1.45	1.72	0.19	21.22	55.51	0.60	0.56	3.24	6.39	0.03	11.23	0.60	0.71	79.84	79.84
	G10-23	2704.7	0.54	44.26	0.06	4.48	11.60	0.15	0.12	0.64	2.22	0.18	2.37	0.13	0.58	n.d.	n.d.
	G10-26	2708.8	1.86	37.41	0.20	8.47	23.80	0.28	0.19	1.22	3.67	0.13	4.48	0.25	0.63	81.29	81.29
Da3	G10-28	2712.5	1.21	14.39	0.31	15.74	43.35	0.59	0.43	2.24	4.86	0.04	8.33	0.48	0.71	80.37	80.37
	G10-30	2720.9	0.78	1.66	0.13	20.43	56.40	0.87	0.42	3.12	6.45	0.06	10.82	0.61	0.70	81.08	81.08
Da1	X29-1	1983.6	0.25	72.19	0.10	1.74	4.70	0.07	0.06	0.26	0.99	0.03	0.92	0.04	0.56	n.d.	n.d.

(*continued on next page*)

Table 1 (*continued*)

Sub-Member	Samples	Depth	TOC (wt %)	Major elements CaO (wt %)	P_2O_5 (wt %)	Al_2O_3 (wt %)	SiO_2 (wt %)	TiO_2 (wt %)	Na_2O (wt %)	K_2O (wt %)	Fe_2O_3 (wt %)	MnO (wt %)	Al (wt %)	Si/Si*	Al/Al*	CIA	CIAcorr
	X29-2	1986.0	0.57	62.49	0.31	3.96	10.16	0.12	0.09	0.60	1.73	0.04	2.10	0.09	0.63	n.d.	n.d.
	X29-3	1991.1	0.48	68.55	0.25	2.39	7.03	0.07	0.10	0.36	1.34	0.04	1.27	0.06	0.57	n.d.	n.d.
Da2	X29-4	1992.9	0.57	2.53	0.13	21.94	55.75	0.85	0.41	3.87	5.97	0.03	11.62	0.60	0.73	79.82	79.82
	X29-6	1996.2	0.41	1.95	0.11	22.95	55.04	0.70	0.46	4.01	5.96	0.03	12.15	0.59	0.74	79.65	79.65
	X29-8	1999.0	0.46	2.10	0.13	22.99	53.87	0.67	0.46	4.16	6.33	0.03	12.17	0.58	0.73	79.23	79.23
	X29-9	2001.0	0.51	27.57	0.12	12.56	30.98	0.44	0.23	2.37	5.18	0.13	6.65	0.33	0.64	79.05	79.05
	X29-10	2002.2	0.62	4.54	0.72	20.58	51.28	0.58	0.30	3.75	7.94	0.04	10.90	0.55	0.66	80.28	80.28
	X29-11	2003.9	0.71	2.75	0.10	20.78	54.72	0.66	0.37	3.71	6.97	0.04	11.00	0.59	0.69	79.85	79.85
	X29-12	2005.5	0.7	9.67	0.37	14.20	55.09	0.35	0.23	1.97	8.89	0.04	7.52	0.55	0.55	83.07	83.07
	X29-13	2006.8	0.68	2.66	0.11	22.23	53.85	0.62	0.38	3.74	7.02	0.04	11.77	0.57	0.70	80.72	80.72
	X29-16	2011.7	3.11	5.23	0.24	19.12	51.50	0.64	0.71	3.82	6.08	0.05	10.12	0.57	0.70	74.68	74.68
	X29-18	2015.2	1.87	0.38	0.07	20.36	56.85	0.64	0.57	3.75	6.24	0.04	10.78	0.63	0.71	78.64	77.40
	X29-21	2020.1	0.89	2.24	0.11	18.80	59.62	0.64	0.61	3.28	5.81	0.02	9.95	0.64	0.71	77.16	77.16
	X29-23	2023.1	1.64	0.41	0.08	19.50	59.10	0.59	0.62	3.37	6.16	0.03	10.32	0.65	0.70	78.85	78.85

1.Si/Si* represents Si/(Si + Al + Fe + Ca).
2.Al/Al* represents Al/(Al + Fe + Mn).
3.CIA is the chemical index of alteration.
4.n.d. means not detected.

highest Al concentrations (mean = 9.57 wt%) and lowest $(La/Yb)_N$ ratios (mean = 1.19) were observed in well G10 (Tables 1 and 2). In the Da2 submember, the Al concentrations ranged from 1.07 to 11.83 wt% and the $(La/Yb)_N$ ratios varied from 1.02 to 1.55 in well PL10, with average values of 9.02 wt% and 1.21, respectively. Similar to the $(La/Yb)_N$ ratios in well PL10, the Al concentrations ranged from 6.65 to 12.17 wt% (mean = 10.41 wt%) in well X29. Compared to those in well PL10 and well X29, the sediments in the Da2 submember in well G10 had lower $(La/Yb)_N$ ratios (varying from 0.74 to 1.22), with an average of only 1.04, and Al concentrations ranging from 2.37 to 11.23 wt% (on average 8.35 wt%) (Tables 1 and 2). Except for well G10, the Al concentrations in Da1 and Da3 submembers are lower than those in Da2 submember, and the $(La/Yb)_N$ ratios in Da1 and Da3 submembers are higher than those in Da2 submember. These observations are not apparent in the Da'anzhai Member of well G10.

5. Discussion

5.1. *Provenance of the major mineral matrix in fine-grained rocks*

The fine-grained rocks of the Da'anzhai Member in the central Sichuan Basin host siliceous, calcareous, and mixed matrices (Fig. 3). The matrix is mainly composed of siliceous and calcareous materials, and their origins can reveal the sedimentation and diagenesis of fine-grained rocks. In the Al-Fe-Mn ternary diagram (Adachi et al., 1986), the provenance of siliceous material in the Da'anzhai Member samples shows a non-hydrothermal origin, with a few samples from well PL10 influenced by hydrothermal fluids (Fig. 8A). Moreover, the Si/(Si + Al + Fe + Ca) values were less than 0.85 and the Al/(Al + Fe + Mn) values deviated from 0.6, suggesting a nonbiological source for siliceous sediments (Table 1; Wedepohl, 1971; Adachi et al., 1986). Meanwhile, a strong relationship between SiO_2 and Al_2O_3 or TiO_2 concentration implies clastic delivery of siliceous material during deposition (Fig. A3). According to the La/Th versus Hf diagram (Fig. 8B) and the ternary diagram of La–Th–Sc (Fig. 8C), the samples are mainly derived from mixed felsic-basic igneous rocks; most of the fine-grained rocks in the study area are characterized by high siliceous content (Fig. 3). Additionally, the low Zr/Sc ratios suggest that the compositions of the samples were primarily controlled by the source rock compositions (Fig. 8D). Hence, the effect of transport recycling was likely to be limited, and the noisy overprints of heterogeneous compositions of source detrital supplies on the CIA values could have been greatly reduced (Mclennan, 1993; Zhang et al., 2021).

The sources of calcareous materials are likely to be biological shells (Fig. 4A-C, and 5C) and recrystallized calcite laminae (Fig. 4C and 5F). Unlike carbonate recrystallization in biological shells (Fig. 5F), the recrystallized calcite laminae may have been caused by fluid flow in the sediments (Wang et al., 2005; Liang et al., 2018).

5.2. *Influence of the sedimentary paleoenvironment on differential OM enrichment*

In the study area, fine-grained rocks were distributed in various sedimentary facies. For example, crystalline shell limestones are mainly deposited on the shell beach core facies and shell beach edge facies, including shore and shallow lakes (Fig. 9; Thompson et al., 2015; Xu et al., 2020). Disorderly distributed shells filled with sparry calcite (Fig. 5A) indicate a sedimentary water body with high energy. Except for the shell beach core facies, a few crystalline shell limestones were deposited in the Da2 submember (Fig. 9; Xu et al., 2020). The fine-grained rocks in the Da2 submember were dominated by shale (Fig. 9). From shell beach core facies to intermediate depth-deep lake facies, crystalline shell limestones decrease and muddy shell limestones, especially shales, are deposited more frequently (Fig. 12; Xu et al., 2020). In the shore lake, a high-energy water environment, fine-grained rocks (muddy shell limestones and shales) are readily influenced by lake

Table 2
Trace elements and rare earth elements in the Da'anzhai Member.

Sub-member	Samples	Trace element														
		La (ppm)	Yb (ppm)	Th (ppm)	Hf (ppm)	Zr (ppm)	Sc (ppm)	Mo (ppm)	U (ppm)	V (ppm)	Ba (ppm)	Cu (ppm)	Ni (ppm)	Zn (ppm)	$(La/Yb)_N$	La/Th
Da1	PL10-1	2.10	0.13	0.45	0.07	n.d.	n.d.	0.58	0.14	2.75	69.30	1.08	0.98	1.68	1.57	4.67
Da2	PL10-2	37.62	2.35	17.37	3.02	115.68	14.088	1.84	2.63	135.30	496.60	33.16	45.46	97.08	1.55	2.17
	PL10-3	5.64	0.45	2.22	0.46	n.d.	n.d.	3.94	0.56	21.16	152.00	8.44	11.14	20.54	1.22	2.54
	PL10-4	32.04	2.58	18.28	3.60	142.18	18.50	0.95	2.86	188.64	735.60	42.46	49.58	152.58	1.20	1.75
	PL10-6	42.36	2.75	20.24	3.02	115.34	14.71	0.97	2.44	114.34	531.80	25.94	38.84	79.54	1.49	2.09
	PL10-7	29.82	2.41	17.43	3.49	135.34	18.68	6.94	2.66	197.64	700.00	46.62	54.36	104.98	1.20	1.71
	PL10-9	26.12	2.31	11.78	3.13	121.10	17.13	7.72	2.71	214.40	758.40	50.96	48.08	119.28	1.10	2.22
	PL10-10	23.84	1.67	6.82	1.85	n.d.	n.d.	1.08	3.41	109.10	432.40	25.92	27.44	67.92	1.38	3.50
	PL10-12	18.82	1.67	9.11	2.50	95.76	12.69	1.19	2.21	140.08	625.60	33.74	45.12	95.70	1.09	2.07
	PL10-15	29.42	2.47	15.01	3.43	135.36	16.72	0.73	2.59	114.08	643.00	41.52	46.36	116.40	1.15	1.96
	PL10-18	23.54	2.23	12.76	3.81	150.30	16.31	1.87	3.12	199.60	679.00	42.38	46.66	122.66	1.02	1.84
	PL10-20	36.00	3.08	18.73	4.05	159.68	17.97	1.78	3.25	93.84	668.20	48.40	52.08	114.80	1.13	1.92
	PL10-21	24.28	2.14	12.24	3.56	140.68	16.00	2.28	3.00	173.30	659.60	42.44	49.82	109.62	1.10	1.98
	PL10-22	40.66	3.40	21.44	4.64	187.26	17.77	11.05	3.14	73.14	667.80	46.02	53.34	123.66	1.16	1.90
	PL10-23	36.68	2.79	17.43	4.14	161.36	13.02	2.62	2.76	131.00	534.00	40.12	42.16	111.02	1.28	2.10
	PL10-25	30.74	2.68	16.56	4.32	175.94	14.63	0.65	3.03	115.88	647.80	43.74	49.20	118.92	1.11	1.86
	PL10-26	4.90	0.42	1.34	0.35	n.d.	n.d.	1.46	0.39	12.69	230.60	6.92	8.88	22.70	1.14	3.65
	PL10-27	36.34	2.87	18.56	3.93	158.84	17.30	1.93	2.59	73.66	643.80	40.56	52.52	137.16	1.23	1.96
	PL10-28	25.66	2.22	10.77	3.13	109.98	11.01	3.04	2.04	112.62	534.80	31.62	36.38	84.00	1.12	2.38
	PL10-30	48.46	3.70	22.16	4.52	181.32	14.29	0.89	3.19	111.30	449.00	40.64	43.00	89.96	1.27	2.19
	PL10-31	42.80	3.32	20.30	3.92	151.02	14.31	1.14	3.37	122.40	443.00	38.56	44.04	88.66	1.25	2.11
	PL10-33	33.08	2.73	17.29	3.50	137.88	14.05	2.86	2.50	108.98	489.80	33.64	41.14	111.80	1.17	1.91
	PL10-34	25.28	2.01	10.75	2.79	105.12	10.35	1.55	1.82	122.14	525.60	36.80	32.74	86.66	1.22	2.35
Da3	PL10-36	2.38	0.15	0.49	0.08	n.d.	n.d.	0.62	0.17	2.98	72.90	1.15	1.02	1.81	1.53	4.81
Da2	G10-11	27.32	2.38	12.27	3.67	128.38	19.73	3.24	3.60	177.86	490.00	40.22	52.34	105.20	1.11	2.23
	G10-12	27.38	2.17	12.27	3.39	121.26	18.67	2.28	1.93	148.96	534.60	40.28	37.36	113.84	1.22	2.23
	G10-13	19.73	1.88	7.29	2.49	84.00	12.97	1.77	1.42	70.12	256.60	19.50	22.54	65.20	1.02	2.71
	G10-15	22.84	1.87	10.23	3.04	105.84	17.70	1.40	0.61	37.38	158.88	10.84	14.73	32.02	1.18	2.23
	G10-18	26.52	2.14	11.46	3.50	119.48	17.91	1.48	2.46	184.46	717.80	41.32	49.08	128.52	1.20	2.31
	G10-23	10.55	1.39	2.45	0.82	n.d.	n.d.	0.43	1.07	61.64	663.20	11.82	10.78	30.62	0.74	4.31
	G10-26	15.06	1.76	4.47	1.43	48.58	9.31	1.00	1.90	118.18	502.20	33.32	36.50	68.16	0.83	3.37
Da3	G10-28	23.24	2.23	9.74	3.32	115.14	15.22	2.36	2.65	186.70	677.40	44.00	51.96	106.26	1.01	2.39
	G10-30	47.58	3.36	18.58	4.64	160.64	18.59	0.77	2.58	201.60	695.60	48.66	51.06	105.38	1.37	2.56
Da1	X29-1	2.99	0.21	1.10	0.24	n.d.	n.d.	1.28	0.34	11.54	101.46	1.74	4.09	5.60	1.39	2.73
	X29-2	6.85	0.48	2.59	0.44	n.d.	n.d.	1.02	0.50	21.36	214.20	5.01	8.18	18.84	1.38	2.65
	X29-3	4.01	0.25	1.39	0.26	n.d.	n.d.	1.48	0.44	17.40	215.40	2.98	4.74	9.76	1.53	2.89
Da2	X29-4	43.80	2.97	21.68	4.09	162.70	18.12	1.01	2.90	113.78	573.00	40.04	50.26	113.56	1.43	2.02
	X29-6	39.22	2.68	19.73	3.67	143.02	19.33	1.54	2.64	192.86	597.80	39.54	53.52	141.46	1.42	1.99
	X29-8	37.14	2.38	18.83	3.25	125.42	18.57	1.13	2.51	93.68	598.60	40.64	56.82	102.36	1.51	1.97
	X29-9	19.20	1.62	8.77	1.91	67.88	8.67	0.95	1.64	93.90	512.40	27.06	30.12	84.10	1.15	2.19
	X29-10	34.72	3.24	13.23	3.16	118.82	17.01	1.48	2.74	93.78	615.00	41.12	57.24	117.26	1.04	2.63
	X29-11	27.80	2.12	13.19	3.19	123.40	17.77	4.73	2.61	189.04	633.20	42.64	50.50	128.76	1.27	2.11
	X29-12	21.60	2.11	7.48	1.73	61.94	11.66	0.87	1.65	95.84	370.00	24.58	36.20	260.20	0.99	2.89
	X29-13	32.80	2.28	16.44	3.14	121.58	18.11	0.79	2.62	130.50	625.40	40.54	49.42	90.06	1.40	1.99
	X29-16	24.78	2.11	11.30	3.00	116.10	16.30	0.34	3.06	211.80	657.60	41.98	49.24	113.54	1.14	2.19
	X29-18	24.38	1.99	10.99	3.10	121.16	17.22	1.14	3.52	205.60	693.40	40.22	48.36	123.22	1.19	2.22
	X29-21	27.34	2.35	14.98	3.61	145.28	16.12	2.41	2.66	66.90	649.80	45.30	53.14	100.54	1.13	1.83
	X29-23	21.62	1.88	11.06	2.95	108.90	15.86	0.65	2.76	201.40	667.20	41.48	48.26	107.32	1.11	1.96

1.n.d. means not detected.

waves, leading to the remobilization of both sediments and bioclasts (Fig. 4B and 5C; Fick et al., 2018). With the weakening of water energy, the shells in fine-grained rocks (muddy shell limestones and shales) became slender and compacted, appearing as laminae in the shallow lake environment (Fig. 4C, 5B, and 9). Occasionally, ostracods were found in the shallow lake shale (Fig. 4D, 5D, and 9). Additionally, a small number of shell fragments were frequently observed in intermediate-depth lakes from the shell beach slope facies (Fig. 9), but

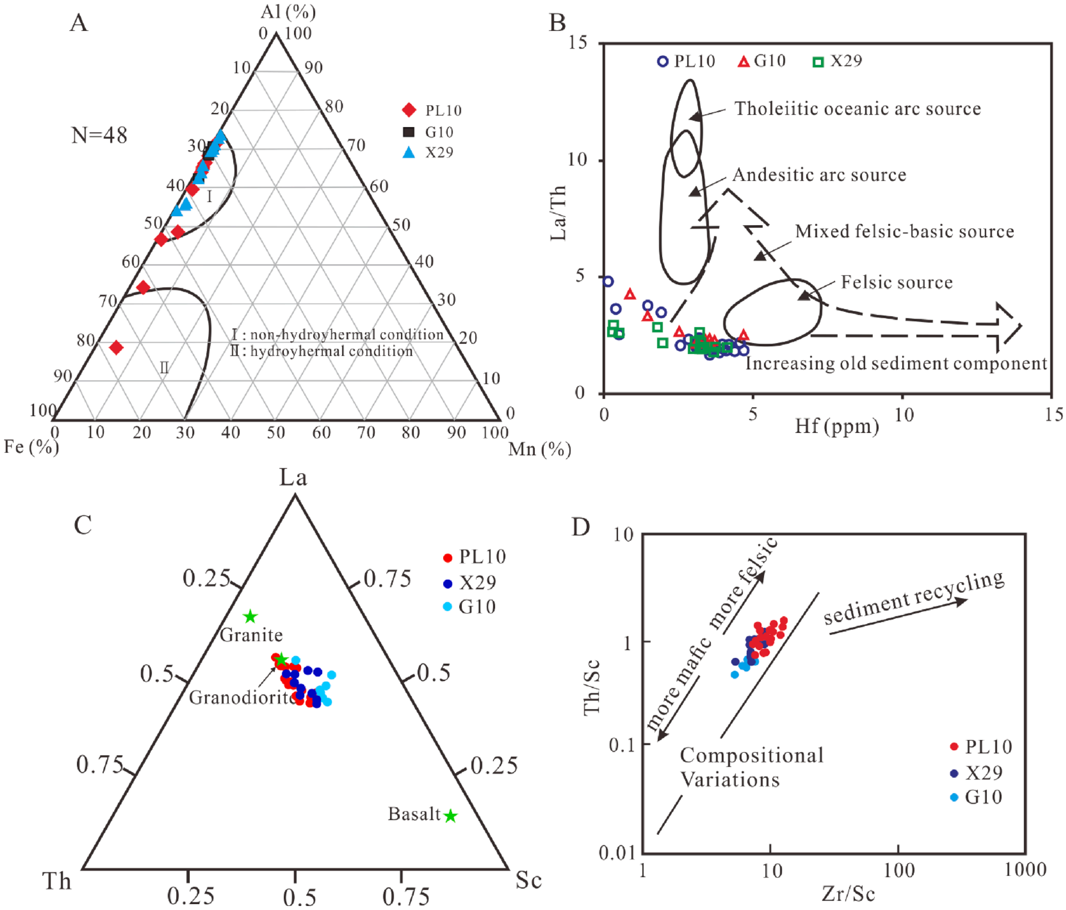

Fig. 8. Provenance and recycling effect of the material matrix in fine-grained rocks. (A) Al-Fe-Mn ternary diagram (Adachi et al., 1986) showing the non-hydrothermal origin of siliceous material in most of the samples; (B) La/Th versus Hf diagram for identifying the source rocks of sedimentary rocks (Floyd and Leveridge, 1987); La-Th-Sc diagram (Cullers and Podkovyrov, 2000); (D) Th/Sc vs. Zr/Sc diagram for discriminating sediment recycling (Mclennan, 1993).

are rare in deep lake sediments (Xu et al., 2020). OM is differentially accumulated in fine-grained rocks of various sedimentary facies, and TOC shows an upward trend from shore lakes to intermediate-depth lakes.

5.2.1. *Paleoredox conditions*

Redox-sensitive trace element (Mo, U, and V) enrichment can provide helpful information on paleoredox conditions. Under oxic conditions, aqueous Mo, U, and V are conservative with little sedimentary uptake, whereas anoxic conditions lead to strong authigenic enrichment relative to the average continental crust, especially for Mo in the presence of free H_2S (Tribovillard et al., 2006). However, V may be released into the overlying water column from reducing sediments deposited beneath an oxic water column (Scholz et al., 2011). Therefore, the co-enrichment of Mo and U, coupled with depletions in V, may indicate deposition from oxic bottom waters adjacent to an anoxic oxygen minimum zone (Zhang et al., 2016). In our samples from the Da'anzhai Member, generally low Mo, U, and V concentrations and their enrichment factors suggest oxic to suboxic depositional conditions (Fig. 7). All samples have Mo concentrations below 15 ppm with an average of 2.0 ppm (Table 2 and Fig. 7), indicating oxic to suboxic conditions (Scott et al., 2008; Jin et al., 2016). Furthermore, the U and V profiles for all three sections show striking similarities with the Mo profiles, and there is no evidence of V depletion associated with U and Mo enrichment (Fig. 7). Therefore, the U and V profiles strongly support the oxic to suboxic conditions indicated by the Mo profiles. Persistent oxic conditions during the Da'anzhai Member deposition enhanced OM degradation, which is not conducive to its preservation. Hence, it is likely that the differential OM enrichment in the Da'anzhai Member is not controlled by redox conditions.

5.2.2. *Paleoproductivity*

Total organic carbon (TOC), P, and micronutrients (Cu, Ni, and Zn) are related to marine primary productivity and have been widely used as proxies for paleoproductivity (see reviews in Tribovillard et al., 2006; Schoepfer et al., 2015). However, the enrichment levels of these proxies can also be affected by multiple environmental factors, particularly redox conditions. Although the measured TOC content does not directly represent the organic carbon flux to the sediment, considering the similar OM maturity and sedimentary environments of our samples, TOC content can be used to reflect paleoproductivity levels. Redox conditions are particularly important for P cycling; oxic conditions would result in enhanced sedimentary P fixation through adsorption to Fe-oxyhydroxides, whereas anoxic conditions would diminish P retention in sediments (Algeo and Ingall, 2007). Our samples were deposited under oxic to suboxic conditions with no evidence for strong anoxia, and lack of significant covariation between P and redox proxies (e.g., Mo) (Fig. 7), implying productivity control on P enrichment in sediments. In terms of micronutrients (Cu, Ni, and Zn), anoxic conditions are generally conducive to their enrichment in sediments (Tribovillard et al., 2006). In our samples, the variation of Cu_{EF}, Ni_{EF}, and Zn_{EF} is similar to that of Mo_{EF}, U_{EF} and V_{EF}, suggesting redox control on their enrichment (Fig. 7).

The increased TOC and P/Al (it is higher than $(P/Al)_{AUCC}$) suggest enhanced primary productivity and nutrient availability in the Da2 submember (Fig. 7). Furthermore, high productivity coincides with high

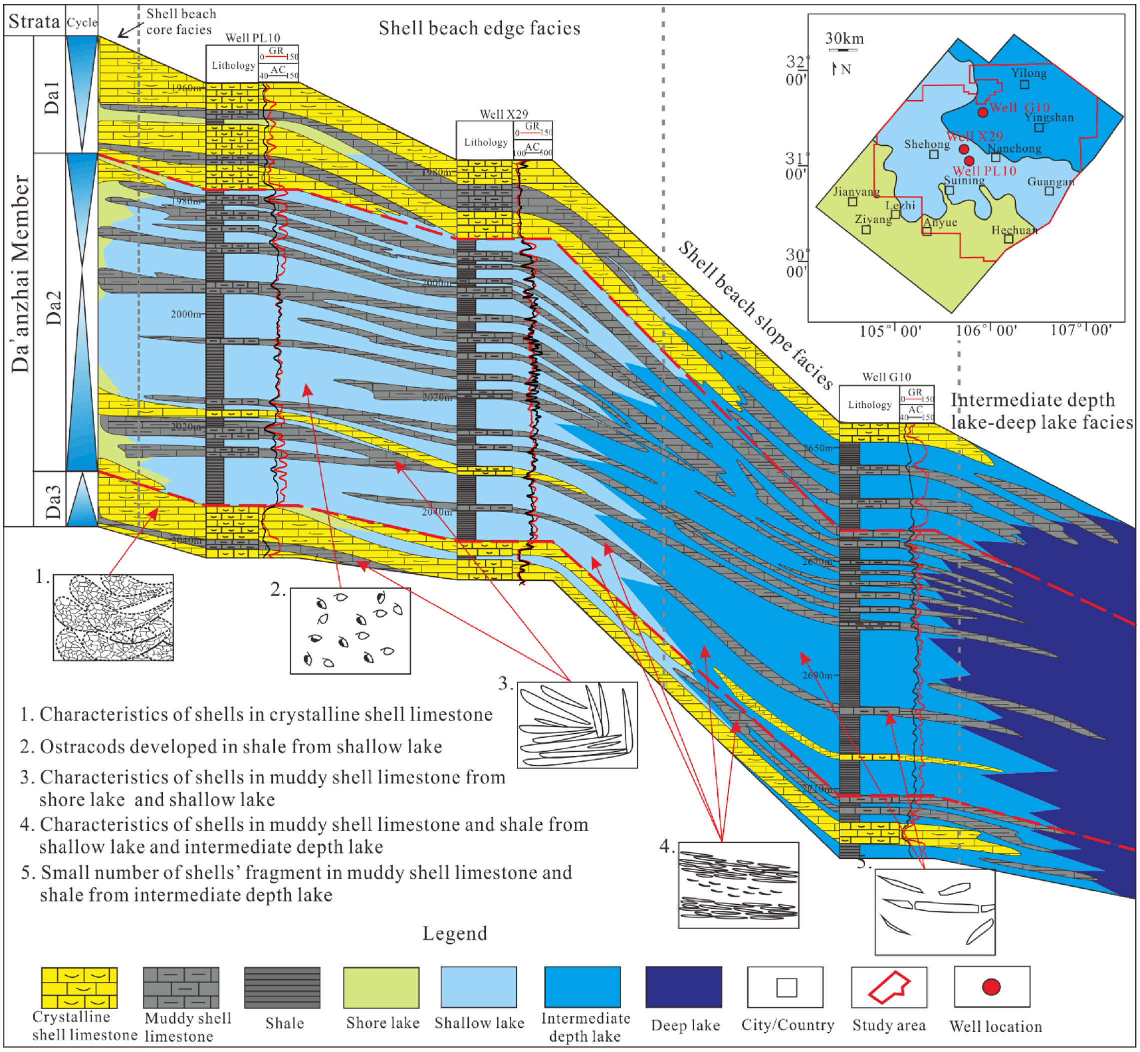

Fig. 9. Sedimentary facies in the Jurassic Da'anzhai Member according to wells PL10, X29, and G10 (modified from Xu et al., 2020).

CIA values in this interval, suggesting that weathering fluxes may have played an important role in the regulating primary productivity. The generally high CIA values (greater than 75) observed in the Da2 submember of all profiles indicate a strong chemical weathering intensity under warm/hot-humid climatic conditions. The enhanced weathering intensity would have increased the weathering influx (e.g., nutrients) into the lake, thereby enhancing the primary production and flux of organic carbon to sediments.

5.2.3. *Clastic input and sedimentation rate*

For the Da2 submember, most samples possessed a high clastic input with high Al concentrations (Table 1 and Fig. 7). Compared to the Da2 submember, the Da1 and Da3 submembers in wells PL10 and X29 had lower clastic inputs (Table 1 and Fig. 7). In shore lakes with high energy, the $(La/Yb)_N$ ratios in Da1 and Da3 submembers in well PL10 reflect a relatively low sedimentation rate (Table 2 and Fig. 7). Meanwhile, in the Da1 submember in well X29, the $(La/Yb)_N$ ratios indicate that the sedimentation rate increased in shallow lakes (Table 2 and Fig. 7). The

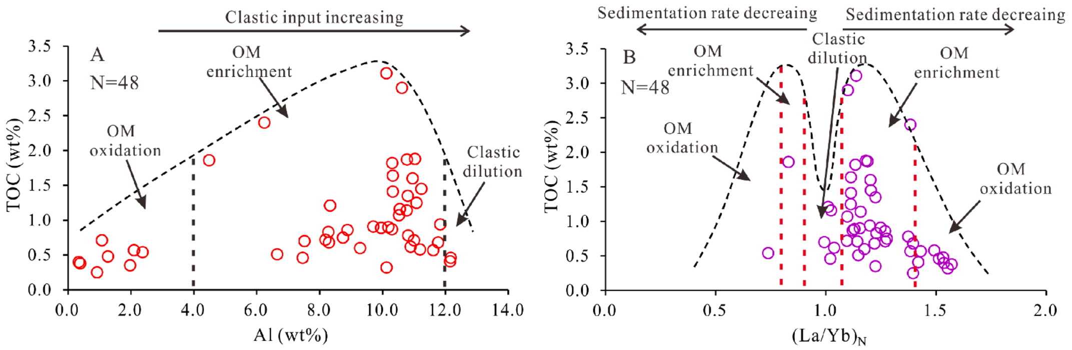

Fig. 10. Influence of clastic input and sedimentation rate on TOC. (A) Al concentration versus TOC showing OM accumulation influenced by increasing clastic input; (B) $(La/Yb)_N$ ratio versus TOC showing OM accumulation influenced by decreasing sedimentation rate (Ibach, 1982; Ding et al., 2015).

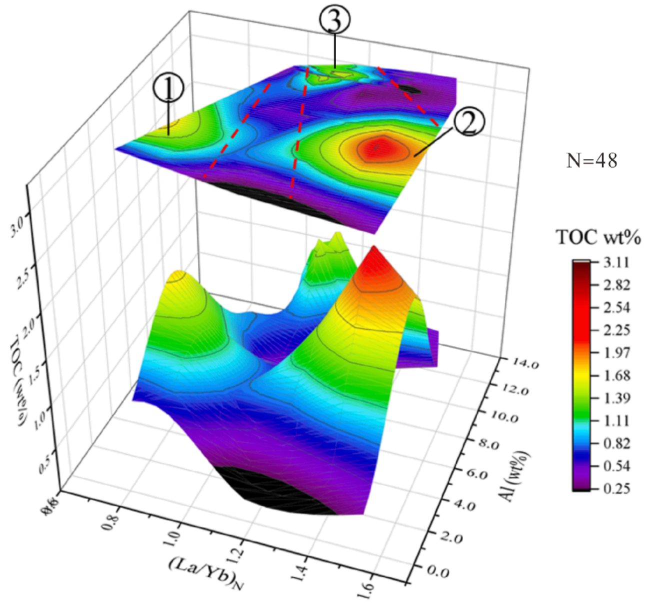

Fig. 11. Relationship between TOC, Al, and $(La/Yb)_N$. The relatively high TOC ($\geq$1.0 wt%) is mainly distributed in three intervals. Interval 1 (Al concentration = 4.0–8.0 wt%, $(La/Yb)_N$ = 0.80–0.95), Interval 2 (Al concentration = 4.0–8.0 wt%, $(La/Yb)_N$ = 1.20–1.55), and Interval 3 (Al concentration = 10.0–13.0 wt%, $(La/Yb)_N$ = 1.00–1.25).

$(La/Yb)_N$ ratios close to 1 indicate a higher sedimentation rate for the Da3 submember in well G10 (Table 2 and Fig. 7). Additionally, the $(La/Yb)_N$ ratios of most samples indicate a high sedimentation rate in the Da2 submember (Table 2 and Fig. 7). From the shore lake to the intermediate-depth lake, the clastic input and sedimentation rates in the study area exhibited increasing trends.

The Al concentrations in more than 45% of the samples were greater than 10 wt% (Table 1), indicating a relatively high clastic input in the Da'anzhai Member. However, a few samples had low Al concentrations, indicating a relatively low clastic input. Based on the relationship between Al and TOC (Fig. 10A), TOC greater than 1.0 wt% can be found in samples with Al concentrations between 4.0 and 12.0 wt%. When the clastic input was high, the sedimentation rate would increase accordingly, resulting in clastic dilution and low TOC concentrations (Ibach, 1982; Ding et al., 2015). When the clastic input was low, the low sedimentation rate may have resulted in prolonged degradation of OM and therefore low TOC concentrations. Hence, a moderate clastic input was conducive to OM accumulation, which prevented clastic dilution and oxidation of OM. In the study area, an Al concentration between 4.0 and 12.0 wt% may be the interval of moderate clastic input and enriched OM (Fig. 10A).

Previous studies have suggested that TOC tends to increase with increasing sedimentation rate (Heath et al., 1977). However, high sedimentation rates (greater than5 cm/ky) also have negative effects on OM accumulation due to clastic dilution (Ibach, 1982; Ding et al., 2015). In this study, the $(La/Yb)_N$ ratio was used as a proxy for sedimentation rate. The $(La/Yb)_N$ ratio was close to 1, corresponding to a high sedimentation rate, which theoretically shows two peaks in the $(La/Yb)_N$ versus the TOC diagram (Fig. 10B). Based on the relationship between $(La/Yb)_N$ and TOC (Fig. 10B), TOC > 1.0 wt% occurred at $(La/Yb)_N$ ratios of approximately 0.8 to 0.9 and 1.1 to 1.4. Within these intervals, OM was protected from clastic dilution and oxidation (Fig. 10B). When the debris is deposited too fast, clastic dilution is prone to occur under high sedimentation rates; however, the OM may be oxidized at low sedimentation rates (Fig. 10B). Additionally, there is a good correlation between clastic input and sedimentary rate (especially in the Well G10), which may indicate that high clastic inputs lead to high sedimentary rates.

5.3. *Differential OM enrichment mechanism*

The relationships among TOC, Al, and $(La/Yb)_N$ in the Da'anzhai Member were simulated using Origin 2018 software (OriginLab, USA). As shown in Fig. 11, the relatively high TOC ($\geq$1.0 wt%) was mainly distributed in three intervals. In Interval 1, the $(La/Yb)_N$ ratios varied

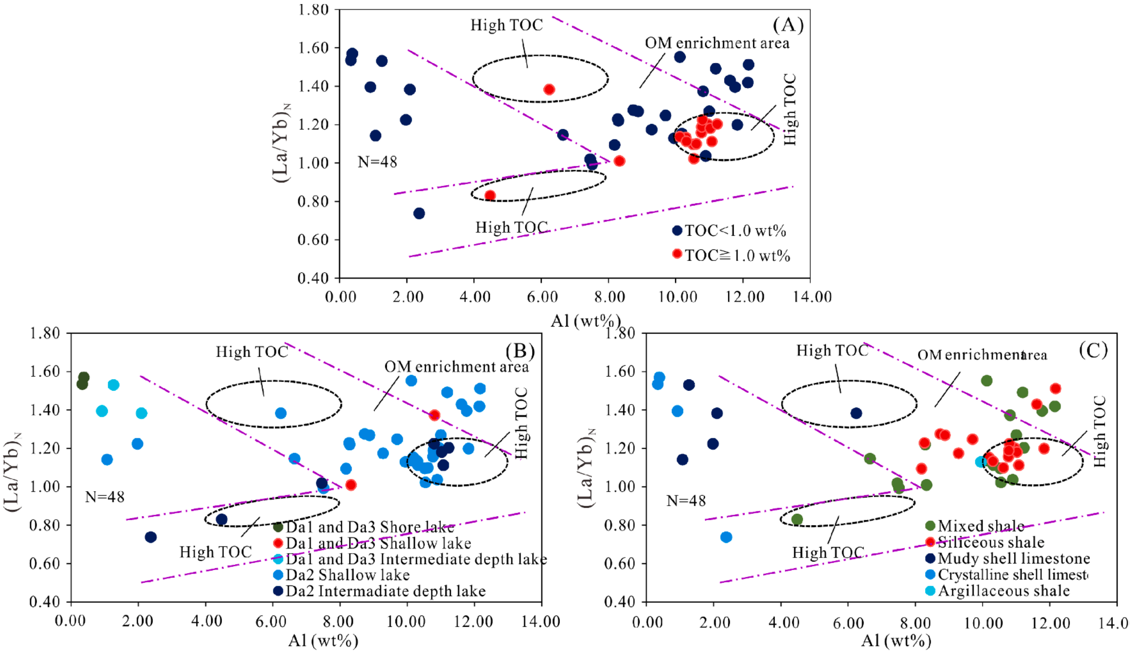

Fig. 12. TOC, sedimentary facies, and lithologies are distributed in the diagram of Al concentration versus $(La/Yb)_N$ ratio. (A) Al concentration versus $(La/Yb)_N$ ratio with different TOC; (B) Al concentration versus $(La/Yb)_N$ ratio with different sedimentary facies; (C) Al concentration versus $(La/Yb)_N$ ratio with different lithologies. Black dotted circles represent the areas with TOC above 1.0 wt%. The area formed by the pink dotted lines is beneficial to OM accumulation. (For interpretation of the references to colour in this figure legend, the reader is referred to the web version of this article.)

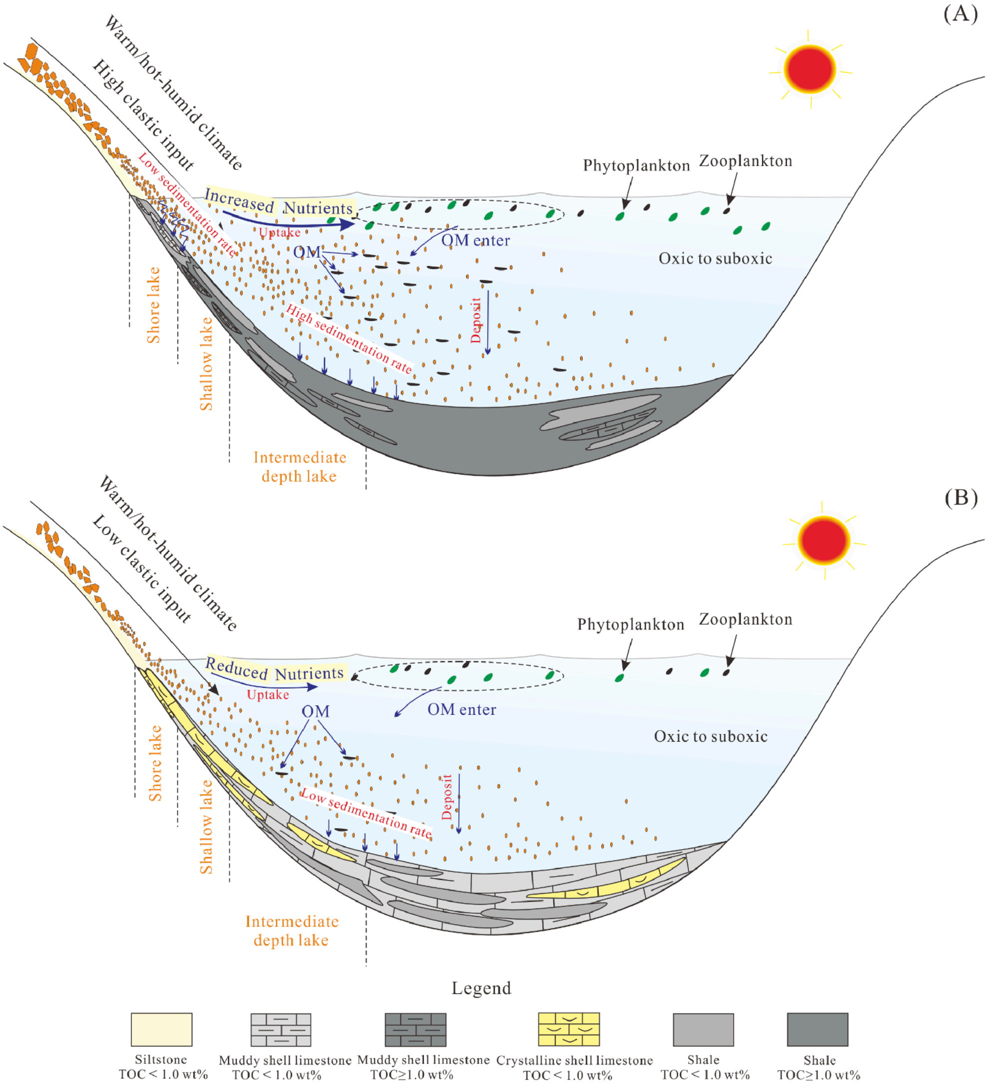

Fig. 13. Schematic sediment deposition with different clastic inputs. (A) Deposition with high clastic input where OM can enter the debris in large amounts; (B) deposition with low clastic input where a small amount of OM enter the debris.

from 0.80 to 0.95 and the Al concentrations ranged from 4.0 wt% to 8.0 wt% (Fig. 11). In Interval 2, the Al concentrations were similar to that in Interval 1, and the $(La/Yb)_N$ ratios varied from 1.20 to 1.55 (Fig. 11). In Interval 3, $(La/Yb)_N$ ratios were close to 1, ranging from 1.00 to 1.25, and Al concentrations ranged from 10.0 wt% to 13.0 wt% (Fig. 11). Therefore, the three intervals with relatively high TOC (>1.0 wt%) in the study area are likely to be controlled by sedimentation rate and clastic input (Fig. 12A).

In our samples of different lithologies, the fine-grained siliceous shales generally have higher TOC contents ($\geq$1.0 wt%) in the Da2 submember (Fig. 12B). The relatively high Al contents (Fig. A3) and $(La/Yb)_N$ values close to 1 (Fig. 12C) of siliceous shales suggest a high clastic input and sedimentation rate during its deposition, which favors the enrichment of OM. For mixed shale with high Al concentrations, the wider range of $(La/Yb)_N$ ratios (Fig. 12C) complicates OM enrichment. Similar to the mixed shales, there is a strong discrepancy in OM content in muddy shell limestone (Fig. 6D) due to low Al concentrations and a wide range of $(La/Yb)_N$ values (Fig. 12C). Additionally, crystalline shell limestones possess low Al concentrations (<4.0 wt%, Fig. 12C) with low TOC content (Fig. 6D). Statistical analysis of argillaceous shale has not been performed in this study due to limited data.

We further propose a model to link the sedimentary paleoenvironment and the differential enrichment of OM, which can be divided into two major types: deposition with high clastic input and low clastic input (Fig. 13). Our integrated model is different from the previous OM accumulation model, which is considered to be mainly controlled by redox conditions (Xu et al., 2017). As Type II kerogen is present in the study area, OM is mainly supplied by phytoplankton and zooplankton. Under oxic to suboxic water column conditions and the warm/hot-humid paleoclimate conditions, the differential OM enrichment in fine-grained rocks of the Da’anzhai Member is controlled by the sedimentation rate and clastic input (Fig. 13). Under warm/hot-humid paleoclimate conditions, (Fig. 13A), the enhanced weathering influx may have increased the nutrient availability in the lake, thereby stimulating primary production. Under high clastic input conditions, the relatively low sedimentation rate in the shore lake setting could have led to the prolonged OM degradation and hence the low TOC contents in muddy shell limestones and shales (Fig. 13A). In contrast, the higher sedimentation rate in the shallow lake and intermediate-depth lake settings would have prevented OM from being oxidized, resulting in the accumulation of OM in fine-grained sediments (Fig. 13A). Under low clastic input conditions, reduced nutrient availability may have limited primary productivity, and low sedimentation rate would have promoted organic matter decomposition, resulting in a low TOC content in fine-grained rocks (Fig. 13B).

6. Conclusions

Our new petrography and geochemical data provide constraints on the differential enrichment of OM in the Jurassic Da'anzhai Member in the central Sichuan Basin. The deposits of crystalline limestone were reduced from shore lakes to intermediate-depth lakes, but muddy shell limestone, especially shale, was deposited more frequently. Among the fine-grained rocks, siliceous shales have higher TOC contents than other types of fine-grained rocks in the Da'anzhai Member. In terms of the sedimentary paleoenvironment, oxic to suboxic water column conditions are unlikely to be the controlling factors of OM enrichment in fine-grained rocks. Certain paleoproductivity, clastic input, and sedimentation rates are beneficial for OM accumulation. Our results reveal that the appropriate sedimentation rate and clastic input is likely to be the key factor for the enrichment of OM in the Da'anzhai Member, which avoids clastic dilution or OM oxidation. In this scenario, OM enrichment typically occurs in siliceous shale with high clastic input and high sedimentation rate, while OM content varies greatly among other lithologies.

CRediT authorship contribution statement

Ziyi Liu: Data curation, Writing – original draft, Methodology, Conceptualization. **Dongxia Chen:** Writing – review & editing, Supervision, Conceptualization. **Wenzhi Lei:** Resources, Formal analysis. **Yang Liu:** Writing – review & editing, Conceptualization, Software. **Guangjie Xie:** Visualization. **Wei Dang:** Investigation. **Xiuxiang Lv:** Investigation. **Sha Li:** Software. **Siyu Yuan:** Software.

Declaration of Competing Interest

The authors declare that they have no known competing financial interests or personal relationships that could have appeared to influence the work reported in this paper.

Acknowledgments

This work was supported by the National Major Science and Technology Projects of China (2016ZX05034-001-005), National Natural Science Foundation of China (Grant No. 41972124, 42102171), and the Fundamental Research Funds for the Central Universities, China (2652019098).

Appendix A. Supplementary material

Supplementary data to this article can be found online at https://doi.org/10.1016/j.jseaes.2022.105319.

References

Adachi, M., Yamamoto, K., Sugisaki, R., 1986. Hydrothermal chert and associated siliceous rocks from the northern Pacific their geological significance as indication od ocean ridge activity. Sed. Geol. 47 (1–2), 125–148.

Algeo, T.J., Ingall, E., 2007. Sedimentary Corg: P ratios, paleocean ventilation, and Phanerozoic atmospheric pO2. Palaeogeogr. Palaeoclimatol. Palaeoecol 256, 130–155.

Blood, D.R., Schlaegle, S., Hefferan, C.M., Vazquez, A., McAllister, D., 2019. Diagenetic Pyrite Morphology in Mudstones of the Upper Ordovician Point Pleasant Limestone, Appalachian Basin: Evidence for Dysoxic Deposition. AAPG Mem. 120, 69–82.

Carvajal-Ortiz, H., Gentzis, T., 2015. Critical considerations when assessing hydrocarbon plays using Rock-Eval pyrolysis and organic petrology data: Data quality revisited. Int. J. Coal Geol. 152, 113–122.

Chalmers, G.R.L., Bustin, R.M., 2008. Lower Cretaceous gas shales in northeastern British Columbia. Part I: geological controls on methane sorption capacity. Bull. Could. Petrol. Geol 56, 1–21.

Chen, C., Wang, J.S., Wang, Z., Peng, Y.B., Chen, X.H., Ma, X.C., Cen, Y., Zhao, J., Zhou, P., 2020. Variation of chemical index of alteration (CIA) in the Ediacaran Doushantuo Formation and its environmental implications. Precambr. Res 347, 1–10.

Chen, S., Zhu, Y., Wang, H., Liu, H., Wei, W., Fang, J., 2011. Shale gas reservoir characterisation: a typical case in the southern Sichuan Basin of China. Energy 36 (11), 6609–6616.

Chen, Y.H., Zhu, Z.W., Zhang, L., 2019. Control actions of sedimentary environments and sedimentation rates on lacustrine oil shale distribution, an example of the oil shale in the Upper Triassic Yanchang Formation, southeastern Ordos Basin (NM China). Mar. Pet. Geol. 102, 508–520.

Chermak, J.A., Schreiber, M.E., 2014. Mineralogy and trace element geochemistry of gas shales in the United States: Environmental implications. Int. J. Coal Geol. 126, 32–44.

Collins, M.J., Bishop, A.N., Farrimond, P., 1995. Sorption by mineral surfaces: Rebirth of the classical condensation pathway for kerogen formation? Geochim. Cosmochim. Acta 59, 2387–2391.

Cullers, R.L., Podkovyrov, V.N., 2000. Geochemistry of the Mesoproterozoic Lakhanda shales in southeastern Yakutia, Russia: implications for mineralogical and provenance control, and recycling. Precambrian Res 104 (1), 77–93.

Dai, J.X., Zou, C.N., Liao, S.M., Dong, D.Z., Ni, Y.Y., Huang, J.L., Wu, W., Gong, D.Y., Huang, S.P., Hu, G.Y., 2014. Geochemistry of the extremely high thermal maturity Longmaxi shale gas, southern Sichuan Basin. Org. Geochem 74, 3–12.

Ding, X.J., Liu, G.D., Zha, M., Huang, Z.L., Gao, C.H., Lu, X.J., Sun, M.L., Chen, Z.L., Liuzhuang, X.X., 2015. Relationship between total organic carbon content and sedimentation rate in ancient lacustrine sediments, a case study of Erlian basin, northern China. J. Geochem. Explor. 149, 22–29.

Elderfield, H., Greaves, M.J., 1982. The rare earth elements in seawater. Nature 296, 214–219.

Feng, R.C., Wu, Y.Y., Yang, G., Yang, J.J., Liu, M., Zhang, T.S., Yue, T., 2015. Storm deposition of the Da'anzhai Member (Jurassic) in Central Sichuan Basin. Acta Sedimentol. Sin. 33 (5), 909–918.

Fick, C., Toldo Jr, E.E., Puhl, E., 2018. Shell concentration dynamics driven by wave motion in flume experiments: Insights for coquina facies from lake-margin settings. Sed. Geol. 374, 98–114.

Fedo, C.M., Nesbitt, H.W., Young, G.M., 2012. Unraveling the effects of potassium metasomatism in sedimentary rocks and paleosols, with implications for paleoweathering conditions and provenance. Geology 23, 921–924.

Fedo, C.M., Nesbitt, H.W., Young, G.M., 1995. Unraveling the effects of potassium metasomatism in depositional rocks and paleosols, with implications for paleoweathering conditions and provenance. Geology 23, 921–924.

Floyd, P.A., Leveridge, B.E., 1987. Tectonic environment of the Devonian Gramscatho Basin, South Cornwall: framework mode and geochemical evidence from turbiditic sandstones. J. Geol. Soc. Lond 144, 181–204.

Goldberg, T., Strauss, H., Guo, Q., Liu, C., 2007. Reconstructing marine redox conditions for the Early Cambrian Yangtze Platform: evidence from biogenic sulphur and organic carbon isotopes. Palaeogeogr. Palaeoclimatol. Palaeoecol 254, 175–193.

Guo, X.S., 2014. Enrichment Mechanism and Exploration Technology of Jiaoshiba block In Fuling Shale Gas Field. Science Press, Beijing, China.

Guo, X.S., Hu, D.F., Li, Y.P., Wei, Z.H., Wei, X.F., Liu, Z.J., 2017. Geological factors controlling shale gas enrichment and high production in Fuling shale gas field. Pet. Explor. Dev. 44 (4), 513–523.

He, C.C., He, S., Guo, X.S., Yi, J.Z., Wei, Z.H., Shu, Z.G., Peng, N.J., 2018. Structural differences in organic pores between shales of the Wufeng Formation and of the Longmaxi Formation's first Member, Jiaoshiba Block, Sichuan Basin. Oil Gas Geol. 39 (3), 472–484.

Heath, G.R., Moore, T.C., Dauphin, J.P., 1977. Organic carbon in deep sea sediments. In: Anderson, N.R., Malahoff, A. (Eds.), The fate of fossil fuel CO_2 in the oceans. 6. Office of Naval Research, Ocean Science and Technology Division, United States, Marine Sicence 605-625.

Haskin, L.A., Wildeman, T.R., Haskin, M.A., 1968. An accurate procedure for the determination of the rare earths by neutron activation. J. Radioanal. Chem. 1 (4), 337–348.

Hu, H.Y., Hao, F., Lin, J.F., Lu, Y.C., Ma, Y.Q., Li, Q., 2017. Organic matter-hosted pore system in the Wufeng-Longmaxi (O_3w–$S_1$1) shale, Jiaoshiba area, Eastern Sichuan Basin, China. Int. J. Coal Geol. 173, 40–50.

Ibach, L.E.J., 1982. Relationship between sedimentation rate and total organic carbon content in ancient marine sediments. AAPG Bull 66, 170–188.

Jarvie, D.M., Hill, R.J., Ruble, T.E., Pollastro, M., 2007. Unconventional shale-gas systems: the Mississippian Barnett Shale of north-central Texas as one model for thermogenic shale-gas assessment. AAPG Bull. 91 (4), 475–499.

Jin, C.S., Li, C., Algeo, T.J., Planavsky, N.J., Cui, H., Yang, X.L., Zhao, Y.L., Zhang, X.L., Xie, S.C., 2016. A highly redox-heterogeneous ocean in South China during the early Cambrian (529–514Ma): Implications for biota-environment co-evolution. Earth Planet. Sci. Lett 441, 38–51.

Jin, C.S., Li, C., Algeo, T.J., Wu, S.Y., Cheng, M., Zhang, Z.H., Shi, W., 2020. Controls on organic matter accumulation on the early-Cambrian western Yangtze Platform, South China. Mar. Pet. Geol. 111, 75–87.

Johannesson, K.H., Lyons, W.B., Bird, D.A., 1994. Rare earth element concentrations and speciation in alkaline lakes from the western USA. Geophys. Res. Lett 21, 773–776.

Jones, B., Manning, D.A.C., 1994. Comparison of geochemical indices used for the interpretation of palaeoredox conditions in ancient mudstones. Chem. Geol. 111, 111–129.

Krumbein, W.C., 1932. The mechanical analysis of fine-grained sediments. J. Sediment. Res. 2 (3), 140–149.

Lei, W.Z., Chen, D.X., Zhang, R., Liu, Z.Y., Zhang, S.M., 2021. Lithological Combination Types and Characteristics of Continental Shale Strata in the Second Sub-Member of Da'anzhai in Central Sichuan. Earth Sci. 46 (10), 3657–3672.

Liang, C., Jiang, Z.X., Yang, Y.T., Wei, X.J., 2012. Shale lithofacies and reservoir space of the Wufeng-Longmaxi Formation, Sichuan Basin, China. Petrol. Explorat. Devel. 39 (6), 736–743.

Liang, C., Cao, Y.C., Liu, K.Y., Jiang, Z.X., Wu, J., Hao, F., 2018. Diagenetic variation at the lamina scale in lacustrine organic-rich shales: Implications for hydrocarbon migration and accumulation. Geochim. Cosmochim. Acta 229, 112–128.

Liu, X., Zhang, J.C., Liu, Y., Huang, H., Liu, Z.Y., 2018. Main factors controlling the wettability of gas shales: A case study of overmature marine shale in the Longmaxi Formation. J. Nat. Gas Sci. Eng. 56, 18–28.

Liu, Z.Y., Chen, D.X., Zhang, J.C., Lv, X.X., Wang, Z.Y., Liao, W.H., Shi, X.B., Tang, J., Xie, G.J., 2019. Pyrite morphology as an indicator of paleoredox conditions and shale gas content of the Longmaxi and Wufeng shales in the middle Yangtze area, South China. Minerals 9 (7), 428.

Liu, Z.Y., Chen, D.X., Chang, S.Y., Wei, X.L., Lv, X.X., Zuo, R.S., Han, M.L., 2021. Influence of the pore structure on the methane adsorption mechanism in the Upper Triassic lacustrine shales from the western Sichuan Basin, China. Energy Fuels 35, 13654–13670.

Liu, Y., Magnall, J.M., Gleeson, S.A., Bowyer, F., Poulton, S.W., Zhang, J.C., 2020. Spatio-temporal evolution of ocean redox and nirogen cycling in the early Cambrian Yangtze ocean. Chem. Geol. 554, 119803.

Macquaker, J.H.S., Adams, A.E., 2003. Maximizing information from fine-grained sedimentary rocks: an inclusive nomenclature for mudstones. J. Sediment. Res. 73 (5), 735–744.

McLennan, S.M., 2001. Relationships between the trace element composition of sedimentary rocks and upper continental crust. Geochem. Geophys. Geosyst. 2 paper number 2000GC000109.

McLennan, S.M., 1993. Weathering and global Denudation. J. Geol 101, 295–303.

Nelson, P.H., 2009. Pore-throat sizes in sandstones, tight sandstones, and shales. AAPG Bull. 93 (3), 329–340.

Nesbitt, H.W., Young, G.M., 1982. Early Proterozoic climates and plate motions inferred from major element chemistry of lutites. Nature 299, 715–717.

Nesbitt, H.W., Young, G.M., 1989. Formation and diagenesis of weathering profiles. J. Geol 97, 129–147.

Panahi, A., Young, G.M., Rainbird, R.H., 2000. Behavior of major and trace elements (including REE) during Paleoproterozoic pedogenesis and diagenetic alteration of an Archean granite near Ville Marie, Quebec. Canada. Geochim. Cosmochim. Acta 64 (13), 2199–2220.

Peischl, J., Karion, A., Sweeney, C., Kort, E.A., Smith, M.L., Brandt, A.R., Yeskoo, T., Aikin, K.C., Conley, S.A., Gvakharia, A., Trainer, M., Wolter, S., R-yerson, T.B., 2016. Quantifying atmospheric methane emissions from oil and natural gas production in the Bakken shale region of North Dakota. J. Geophys. Res. Atmosph. 121 (10), 6101–6111.

Pi, D.H., Liu, C.Q., Shields-Zhou, G.A., Jiang, S.Y., 2013. Trace and rare earth element geochemistry of black shale and kerogen in the early Cambrian Niutitang Formation in Guizhou province, South China: Constraints for redox environments and origin of metal enrichments. Precambr. Res. 225, 218–229.

Qiu, Z., He, J.L., 2021. Depositional environment changes and organic matter accumulation of Pliensbachian-Toarcian lacustrine shales in the Sichuan basin, SW China. J. Asian Earth Sci.

Raiswell, R., Buckley, F., Berner, R.A., Anderson, T.F., 1988. Degree of pyritization of iron as a paleoenvironmental indicator of bottom-water oxygenation. J. Sediment. Petrol. 58, 812–819.

Rieu, R., Allen, P., Plötze, M., Pettke, T., 2007. Climatic cycles during a Neoproterozoic“snowball” glacial epoch. Geology 35, 299–302.

Rimmer, S.M., Thompson, J.A., Goodnight, S.A., Robl, T.L., 2004. Multiple controls on the preservation of organic matter in Devonian-Mississippian marine black shales: geochemical and petrographic evidence. Palaeogeogr. Palaeoclimatol. Palaeoecol. 215, 125–154.

Ross, D.J.K., Bustin, R.M., 2009. Investigating the use of sedimentary geochemical proxies for paleoenvironment interpretation of thermally mature organic-rich strata: Examples from the Devonian-Mississippian shales, Western Canadian Sedimentary Basin. Chem. Geol. 260 (1–2), 1–19.

Schieber, J., 2016. Mud re-distribution in epicontinental basins-exploring likely processes. Mar. Pet. Geol. 71, 119–133.

Schoepfer, S.D., Shen, J., Wei, H., Tyson, R.V., Ingall, E., Algeo, T.J., 2015. Total organic carbon, organic phosphorus, and biogenic barium fluxes as proxies for paleomarine productivity. Earth-Sci. Rev 149, 23–52.

Scholz, F., Hensen, C., Noffke, A.N., Rohde, A.N., Liebetrau, V., Wallmann, K., 2011. Early diagenesis of redox-sensitive trace metals in the Peru upwelling area: Response of ENSO-related oxygen fluctuations in the water column. Geochim. Cosmochim. Acta 75 (22), 7257–7276.

Scott, C., Lyons, T.W., Bekker, A., Shen, Y., Poulton, S.W., Chu, X., Anbar, A.D., 2008. Tracing the stepwise oxygenation of the Proterozoic biosphere. Nature 452, 456–459.

Scott, C., Slack, J.F., Kelley, K.D., 2017. The hyper-enrichment of V and Zn in black shales of the Late Devonian-Early Mississippian Bakken Formation (USA). Chem. Geol 452, 24–33.

Song, L.S., Bhattacharya, S., Webb, Z., Fowler, A., Lee, V., 2021. Preservation of organic carbon in the Cretaceous Hue Shale on the North Slope of Alaska: Insights from pyrite morphology. Int. J. Coal Geol. 235, 103678.

Sonnenberg, S.A., Pramudito, A., 2009. petroleum geology of the giant Elm Coulee field, Williston Basin. AAPG Bull. 93 (9), 1127–1153.

Speight, J.G., 2013. Shale Gas Production Processes. Gulf Professional Publishing 1–23.

Sun, C.X., Nie, H.K., Dang, W., Chen, Q., Zhang, G.R., Li, W.P., Lu, Z.Y., 2021. Shale gas exploration and development in China: current status, geological challenges, and future directions. Energy Fuels 35, 6359–6379.

Thompson, D.L., Stilwell, J.D., Hall, M., 2015. Lacustrine carbonate reservoirs from Early Cretaceous rift lakes of Western Gondwana: Pre-Salt coquinas of Brazil and West Africa. Gondwana Res. 28, 26–51.

Tian, Z.P., Song, X.M., Wang, Y.J., Ran, Q.Q., Liu, B., Xu, Q.L., Yang, L., 2017. Classification of lacustrine tight limestone considering matrix pores or fractures: A case study of Da’anzhai Member of Jurassic Ziliujing Formation in central Sichuan Basin, SW China. Petrol. Explorat. Devel. 44 (2), 234–246.

Tribovillard, N., Algeo, T.J., Lyons, T., Riboulleau, A., 2006. Trace metals as paleoredox and paleoproductivity proxies: an update. Chem. Geol. 232, 12–32.

Tyson, R.V., 2001. Sedimentation rate, dilution, preservation and total organic carbon: some results of a modelling study. Org. Geochem. 32, 333–339.

Wang, G.M., Ren, Y.J., Zhong, J.H., Ma, Z.P., Jiang, Z.X., 2005. Genetic analysis on lamellar calcite veins in Paleogene black shale of the Jiyang Depression. Acta Geol. Sin. 79 (6), 834–838.

Wedepohl, K.H., 1971. Environmental influences on the chemical composition of shales and clays. Phys. Chem. Earth. 8, 307–333.

Wilkin, R.T., Barnes, H.L., Brantley, S.L., 1996. The size distribution of framboidal pyrite in modern sediments: An indicator of redox conditions. Geochim. Cosmochim. Acta 60, 3897–3912.

Xu, Q.L., Hao, F., Ma, Y.S., Liu, B., Song, X.M., 2020. Effects of the matrix on the oil production of supertight limestone in a lacustrine mixed sedimentary environment: The case of the Jurassic Da’anzhai member in the central Sichuan Basin, China. Marine Petrol. Geol. 121, 104583.

Xu, Q.L., Liu, B., Ma, Y.S., Song, X.M., Wang, Y.J., Xin, X.K., Chen, Z.X., 2017a. Controlling factors and dynamical formation models of lacustrine organic matter accumulation for the Jurassic Da’anzhai Member in the central Sichuan Basin, southwestern China. Mar. Pet. Geol. 86, 1391–1405.

Xu, Q.L., Liu, B., Ma, Y.S., Song, X.M., Wang, Y.J., Chen, Z.X., 2017b. Geological and geochemical characterization of lacustrine shale: A case study of the Jurassic Da’anzhai member shale in the central Sichuan Basin, southwest China. J. Nat. Gas Sci. Eng. 47, 124–139.

Yang, G., Huang, D., Huang, P.H., Yan, W.P., Yang, T.Q., Dai, H.M., Lin, J.P., 2017a. Control factors of high and stable production of Jurassic Da’anzhai Member tight oil in central Sichuan Basin, SW China. Petrol. Explorat. Devel. 44 (5), 866–875.

Yang, R., He, S., Hu, Q.H., Hu, D.F., Yi, J.Z., 2017b. Geochemical characteristics and origin of natural gas from Wufeng-Longmaxi shales of the Fuling gas field, Sichuan Basin (China). Int. J. Coal Geol. 171, 1–11.

Yang, T., Gao, Y.C., Liu, K.Y., Zhou, L.L., Jin, J.H., 2019. Origin of deep-water fine-grained sediments as revealed from the Lower Cretaceous rifting basin sequence in the Lingshan Island, Yellow Sea, Eastern China. J. Asian Earth Sci. 186, 104065.

Yang, Z., Hou, L.H., Tao, S.Z., Cui, J.W., Wu, S.T., Lin, S.H., Pan, S.Q., 2015. Formation and “sweet area” evaluation of liquid-rich hydrocarbons in shale strata. Pet. Explor. Dev. 42 (5), 609–620.

Yu, Y.M., Li, P.P., Guo, R.X., Zhao, Y.Z., Li, S., Zou, H., 2021. Upwelling-induced organic matter enrichment of the Upper Permian Dalong Formation in the Sichuan Basin, SW China and its palaeoenvironmental implications. Palaeogeogr. Palaeoclimatol. Palaeoecol. 576, 110510.

Yuan, X.J., Lin, S.H., Liu, Q., Yao, J.L., Wang, L., Guo, H., Deng, X.Q., Cheng, D.W., 2015. Lacustrine fine-grained sedimentary features and organic-rich shale distribution pattern: a case study of Chang 7 Member of Triassic Yanchang Formation in Ordos Basin, NW China. Petrol. Explorat. Devel. 42 (1), 34–43.

Zeng, S.Q., Wang, J., Fu, X.G., Chen, W.B., Feng, X.L., Wang, D., Song, C.Y., Wang, Z.W., 2015. Geochemical characteristics, redox conditions, and organic matter accumulation of marine oil shale from the Changliang Mountain area, northern Tibet, China. Mar. Pet. Geol. 64, 203–221.

Zhai, L.N., Wu, C.D., Ye, Y.T., Zhang, S.C., Wang, Y.Z., 2018. Fluctuations in chemical weathering on the Yangtze Block during the Ediacaran-Cambrian transition: Implications for paleoclimatic conditions and the marine carbon cycle. Palaeogeogr. Palaeoclimatol. Palaeoecol. 490, 280–292.

Zhang, G.J., Chen, D.Z., Huang, K.J., Liu, M., Huang, T.Y., Yeasmin, R., Fu, Y., 2021. Dramatic attenuation of continental weathering during the Ediacaran-Cambrian transition: Implications for the climatic-oceanic-biological co-evolution. Global Planetary Chang 203, 103518.

Zhang, S., Wang, X., Wang, H., Bjerrum, C.J., Hammarlund, E.U., Costa, M.M., Connelly, J.N., Zhang, B., Su, J., Canfield, D.E., 2016. Sufficient oxygen for animal respiration 1,400 million years ago. PNAS 113, 1731–1736.

Zhang, Y., Horsfield, B., Hou, D., Noah, M., Yang, S., 2019. Impact of hydrothermal activity on organic matter quantity and quality during deposition in the Permian Dalong Formation, Southern China. Mar. Pet. Geol. 110, 901–911.

Zou, C.N., Qiu, Z., Poulton, S.W., Dong, D.Z., Wang, H.Y., Chen, D.Z., Lu, B., Shi, Z.S., Tao, H.F., 2018. Ocean euxinia and climate change “double whammy” drove the Late Ordovician mass extinction. Geology 46 (6), 535–538.

Zou, C.N., Yang, Z., Wang, H.Y., Dong, D.Z., Liu, H.L., Shi, Z.S., Zhang, B., Sun, S.S., Liu, D.X., Li, G.Z., Wu, S.T., Pang, Z.L., Pan, S.Q., Yuan, T.L., 2019. “ Exploring petroleum inside source kitchen” : Jurassic unconventional continental giant shale oil & gas field in Sichuan basin, China. Acta Geologica Sinica 93 (7), 1551–1562.